Acrylate-based slurry development and evaluation for digital light processing of zirconia ceramics

E. Willems[a,b], F. Zhang[a,b], E. Koos[c], B. Van Meerbeek[b], J. Vleugels[a]

[a]KU Leuven, Department of Materials Engineering, Kasteelpark Arenberg 44, B-3001 Leuven, Belgium.

[b]KU Leuven, Department of Oral Health Sciences, BIOMAT - Biomaterials Research group & UZ Leuven, Dentistry, Kapucijnenvoer 7 block a, B-3000 Leuven, Belgium.

[c]KU Leuven, Department of Chemical Engineering, Celestijnenlaan 200J, B-3001 Leuven, Belgium.

Corresponding author: Evita Willems, evita.willems@hotmail.com

Keywords: Zirconia, Stereolithography, Digital light printing, Mechanical properties, Slurry formulation

Willems Evita: Conceptualization. Methodology, Validation, Formal Analysis, Investigation, Writing - Original Draft, Visualization. **Zhang Fei**: Conceptualization, Methodology, Writing - Review & Editing, Supervision, Funding acquisition. **Koos Erin**: Methodology, Writing - Review & Editing. **Van Meerbeek Bart**: Conceptualization, Supervision, Writing - Review & Editing, Funding acquisition. **Vleugels Jef**: Conceptualization, Methodology, Supervision, Writing- Review & Editing, Funding acquisition.

Abstract

The critical steps to produce high-quality zirconia (ZrO_2) ceramics using digital light processing (DLP) are slurry development and tailoring the printing parameters and the post-processing. This paper provides a comprehensive evaluation of experimentally developed slurries containing 3Y-TZP powder, acrylate monomers, diluents, photoinitiator, dispersant and surface energy-reducing agent for DLP of 3Y-TZP, along with a performance assessment of as-printed and as-sintered ZrO_2 ceramics. The viscosity, curing behaviour, stability and thermal debinding characteristics of acrylate-based ZrO_2 slurries were assessed. A speedmixed acrylate-based slurry with 48 vol% 3Y-TZP powder allowed to obtain crack-free and nearly fully dense 3Y-TZP parts. The printed ceramics revealed an anisotropic shrinkage during sintering, which was highest along the building direction (25.2±0.3%) and a decreased printing layer thickness of 15 µm improved the sintered bending strength. The surface roughness varied from 0.35±0.11 µm in plane to 5.77±0.35 µm along the building direction.

Abbreviations

Abbreviation	Description
AM	Additive manufacturing
BAPO	phenylbis (2,4,6-trimethylbenzoyl) phosphine oxide
BD	building direction
CAD/CAM	computer-aided design and computer-aided manufacturing
C_d	Curing depth
DIW	direct ink writing
DLP	digital light processing
E	Young's modulus
E_d	Energy dose
E_c	Critical exposure energy
FFF	Fused filament fabrication
HDDA	1,6 hexanediol diacrylate
HIN	Slurry containing HDDA, IBOA, NGPDA and PPG-400 in a 1:1:1:1 weight ratio
HINP	Slurry containing HDDA, IBOA, NGPDA and PPG-400 in a 1:1:1:1 weight ratio, with a solid load of 48 vol% (84.47 wt%) ZrO_2, 3 wt% Disperbyk-111 relative to the ceramic powder

	content, 25 wt% PPG-400 relative to the amount of monomer and diluent in the slurry, and 0.33 wt% BAPO relative to the monomer content.
H_V	Vickers hardness
IBOA	isobornyl acrylate
K_{IC}	Indentation fracture toughness
LPBF	laser powder bed fusion
LS	laser sintering
m	Weibull modulus
MJ	Material jetting
NGPDA	neopentyl glycol propoxylate diacrylate
PPA	polypropylene glycol acrylate
PEG	polyethylene glycol
PPG	polypropylene glycol
TPGDA	tripropylene glycol diacrylate
S_d	Sensitivity
SERA	BYK-UV 3500
SLA	stereolithography
VP	vat polymerization
ZrO_2	zirconia
2SERA	HINP slurry with 2 wt% SERA
3Y-TZP	3 mol% yttria-stabilized zirconia
3-pt	3-point
4-pt	4-point
θ	water contact angle
σ_m	Average bending strength
σ_0	Characteristic bending strength

1. Introduction

ZrO_2-based ceramics and specifically 3 mol% yttria-stabilized zirconia (3Y-TZP) are widely used because of their high bending strength (1000 MPa), hardness (12-13 GPa) and toughness (4-7 MPa $m^{1/2}$) along with their corrosion and abrasion resistance, biocompatibility and more aesthetically pleasing appearance than metal [1]. Because of these properties, 3Y-TZPs are used in many applications like aerospace [2], dental [3] thermal barriers, devices under high wear and in machining [4]. Conventional manufacturing processes using milling, slip casting and injection moulding are costly, wasteful, time consuming and are limited in the detailed and complex features they can manufacture. Additive manufacturing (AM) was introduced more than 30 years ago as a new manufacturing method to produce 3D objects with complex geometries using the layerwise deposition of powder, cured liquids or sheets of material [5]. AM is currently evolving rapidly in a wide range of industries from aerospace to biomedical applications [6,7] with the use of AM in the dental field being one of the fastest growing [8,9]. Although it is now possible to create components out of a wide range of materials like polymers, metals and ceramics, AM of ceramics is still in its infancy. It is not yet widely adopted in industry due to the insufficient performance of the printed and sintered materials and the need for improved feedstock materials. A wide range of AM techniques exists. Oxide ceramics are often produced using indirect printing techniques, in which a green body is printed that still must be debound and sintered. Direct AM techniques like laser sintering (LS) and laser powder bed fusion (LPBF) of ceramics are reported to produce thermally cracked materials with a high surface roughness [10–12]. For indirect manufacturing techniques, vat polymerization (VP), material jetting (MJ) and extrusion-based techniques like direct ink writing (DIW) and fused filament fabrication (FFF) exist. Of all AM techniques, vat polymerization (VP) is considered one of the most promising [13,14]. VP uses a photopolymeric ceramic slurry composed of ceramic powder, photocurable monomers and a photoinitiator to build a material in a layerwise fashion by curing the slurry by either scanning the surface with a laser (stereolithography; SLA) or projecting the shape using a digital light processor (digital light processing; DLP). DLP allows for parallel production and faster

upscaling, increasing printing productivity. The critical challenges of DLP of 3Y-TZP are the production of a slurry that fulfils all the requirements and optimizes the debinding of the green part. The ceramic suspensions must have a high solid loading to obtain dense parts with concomitant high mechanical performance. The minimal solid load was estimated to be 40 vol% for stereolithography slurries to obtain crack-free sintered ceramics by Griffith et al. (1996) [15]. A higher solid load will also decrease the anisotropic shrinkage issue, which introduces internal stresses [16]. The highly solid loaded slurries need to have low viscosity and shear-thinning behaviour, to allow dispensing or coating of the slurry during printing [15,17]. The most time-consuming and important step in DLP or SLA of ceramics is the debinding. The cured photopolymer binder in the printed green part is removed by either a solvent extraction step and/or a thermal heating process, after which the brown part can be sintered to obtain the final ceramic. Control of the formation of the volatile gases produced through the oxidation or pyrolysis of the polymer binder is important to avoid crack formation and delamination of the ceramics [18]. This step is critical, because ceramic slurries made for DLP contain a significantly higher amount of resin than conventional slurries for colloidal processing [19]. Besides the ceramic powder, the main ingredient of the slurries are monomers, oligomers and diluent. Acrylates are commonly used for VP slurries due to the large variety of commercially available acrylates, the relative low cost and their fast polymerization behaviour upon activation [20]. The addition of a non-reactive diluent can improve defect-free debinding of 3D printed ceramic materials [19]. The main defects reported for DLP- and SLA-manufactured ceramics are (micro)porosities, agglomerates, handling and surface defects and cracks along the layers. Even though some defects could be observed, flexural and biaxial strengths close to that of conventionally manufactured 3Y-TZP have been reported [21–24]. Nakai *et al.* (2021) [25] assessed the performance of 3Y-TZP discs printed by three commercially available VP technologies and determined that the mechanical performance and microstructure can be close to CAD/CAM-milled 3Y-TZP. However, none of the aforementioned reports discussed in detail the composition or mixing procedure of the slurries. The mechanical performance of complex dental parts in a clinical application might be different from the performance of standardized bending bars and discs. Several studies have focused on using either DLP or SLA to create 3Y-TZP dental crowns or prostheses and analysed the accuracy of their final sintered dimensions [26–29]. SLA allowed to print highly accurate dental crowns, but control of the shrinkage behaviour is important [27–29]. Several defects related to the printing process and the supports could be observed on the surface and in the bulk, which will likely influence the mechanical strength of these ceramic parts [29,30]. All of these studies show that AM of ceramics has rapidly progressed in the past years. The main remaining challenges of additive manufacturing are the production of high-strength, reliable ceramics that have the same dimensional accuracy and surface finish as subtractive manufacturing or cast materials.

Since literature reports do not often discuss the exact formulation of zirconia-based resin in detail, the present work focusses on the slurry composition, which was optimised by judicious addition of diluents, dispersants, photoinitiator and other additives. The slurry-preparation procedure was optimized, the DLP-printing parameters were fine-tuned towards crack-free near full density ceramics, and a proper thermal debinding cycle was defined and evaluated. The microstructure, surface roughness, mechanical properties (Vickers hardness, indentation fracture resistance, Young's modulus and flexural strength) of the sintered ceramics were analysed. The objective of this work is to elucidate the influence of each resin component on the properties of the resin, prints and sintered ceramic.

2. Materials and methods

2.1 **Composition of photocurable slurries**

Spray-dried 3 mol% yttria-stabilized zirconia (3Y-TZP) ZrO_2 (TZ-3YS-E, Tosoh, Tokyo, Japan) was used as starting powder, characterized by a specific surface area of 7±2 m^2/g, a crystallite size of 90 nm and a spherical agglomerate size of ~60 µm.

The acrylates used are 1,6 hexanediol diacrylate (HDDA; Sigma Aldrich, Burlington, MA, USA), isobornyl acrylate (IBOA; Sigma Aldrich) and neopentyl glycol propoxylate diacrylate (NGPDA; Sigma Aldrich). HDDA is a typical low-viscosity diluent monomer commonly used for DLP slurries. IBOA and NGPDA have low contractility, allowing for lower polymerization shrinkage. IBOA is highly reactive, while NGPDA is also a low viscosity monomer. A slurry containing equal weight of each monomer was used throughout this work, referred to as HIN based slurry.

The following slurry composition variables were subsequently investigated, as shown in the schematic of the general approach in DLP slurry development in Figure 1.

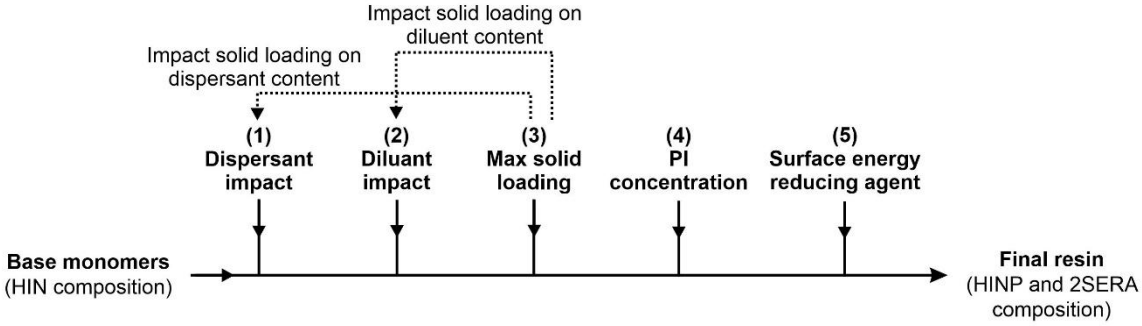

Figure 1. Schematic of the general approach in DLP slurry development used. The dashed lines show the feedback loops to the tests that were repeated once the ideal solid loading (48 vol%) was determined. These feedback loops were not discussed in this paper.

(1) Influence of dispersant nature and content: 0.1-8 wt% (relative to the ZrO_2 solid load) of the following dispersants: KD1, KD4 and KD24 (Croda, Snaith, United Kingdom) and Disperbyk-111 and Disperbyk-180 (BYK, Wesel, Germany). They were tested in 40 vol% ZrO_2 containing HIN slurries with a fixed diluent content to homogeneously disperse the ceramic-powder particles, limiting the slurry viscosity.

(2) Influence of different diluents and extra reactive monomers: 48 vol% ZrO_2 containing HIN slurries without or with 33 wt% of diluent (with respect to the amount of monomer and diluent in the slurry) were effectively printed. According to the results from (1) step, the dispersant (Disperbyk-111) content was fixed at 3 wt%. Reactive monomer-based diluents, including tripropylene glycol diacrylate (TPGDA; Sigma Aldrich) or, polypropylene glycol acrylate (PPA; Sigma Aldrich), and non-reactive diluents including polyethylene glycol (PEG; Sigma Aldrich) or polypropylene glycol (PPG; Sigma Aldrich) were studied. Their influence on the printing behaviour and especially the crack-free debinding potential of the printed slurry were investigated.

(3) The ceramic solid load of the HIN paste, with optimal type and amount of dispersant from (1) and diluent from (2), was maximized based on viscosity measurements.

(4) Influence of the photoinitiator concentration in the optimized 48 vol% ZrO_2 containing HIN paste with 3 wt% Disperbyk-111 and 25 wt% PPG-400: phenylbis (2,4,6-trimethylbenzoyl) phosphine oxide (BAPO; Sigma Aldrich) was used as photoinitiator in concentrations of 0.33-1 wt% relative to the monomer to optimize the curing behaviour based on curing curves.

(5) The influence of the addition of a surface energy reducing agent on the printing and curing of the optimized paste was assessed to minimize edge delamination effects.

An overview of the investigated slurries, along with their nomenclature, is given in Table 1.

Table 1. Composition (wt%) of designed slurries used for slurry characterization

Slurry* → / Compounds ↓		HIN 40 vol% ZrO_2	HIN 48 vol% ZrO_2	HIN-33TPGDA	HIN-33PPA	HIN-33PEG-200	HIN-33PPG-400	HIN-33PPG-1000	HIN-33PPG-2000
Base acrylates	**HDDA**	5.90	4.31	2.89					
	IBOA	5.90	4.31	2.89					
	NGPDA	5.90	4.31	2.89					
Acrylates	**TPGDA**			4.28					
	PPA				4.28				
Diluent	**PEG-200**					4.28			
	PPG-400						4.28		
	PPG-1000							4.28	
	PPG-2000								4.28
Photoinitiator	**BAPO**	0.04							
Dispersant	**Disperbyk-111**	2.40	2.53						
ZrO_2 powder	**TZ-3YS-E**	79.84	84.46						

*The 33 in the slurry code refers to the 33 wt% diluent content (with respect to the amount of monomer (HIN) and diluent in the slurry)

The final slurry (HINP) used for ceramic object printing contained HDDA, IBOA, NGPDA and PPG-400 in a 1:1:1:1 weight ratio, with a solid load of 48 vol% (84.47 wt%) ZrO_2, 3 wt% Disperbyk-111 relative to the ceramic powder content, 25 wt% PPG-400 relative to the amount of monomer and diluent in the slurry, and 0.33 wt% BAPO relative to the monomer content. The effect of BYK-UV 3500 (SERA; BYK) as a surface energy reducing agent was additionally investigated in 2SERA slurry. The composition of the slurries used for printing bending bars for mechanical characterization are summarized in Table 2.

Table 2. Composition (wt%) of designed slurries used for mechanical characterization

Compounds		Slurry	
		HINP	**2SERA**
Base acrylates	**HDDA**	3.24	3.16
	IBOA	3.24	3.16
	NGPDA	3.24	3.16
Diluent	**PPG-400**	3.24	3.16
Surface energy reducing agent	**SERA**	0	0.26
Photoinitiator	**BAPO**	0.04	0.04
Dispersant	**Disperbyk-111**	2.53	2.53
ZrO_2 powder	**TZ-3YS-E**	84.47	84.45

2.2 Slurry preparation

The HINP and 2SERA slurries (Table 2) used for printing were mixed in a stepwise fashion (Figure 2). First, 75.8 g of ZrO_2 powder and the respective amount of dispersant were mixed using a SpeedMixer (Hauschild, Hamm, Germany) for 2 min at 2000 rpm using 90 g of 2 mm diameter 3Y-TZP milling balls (grade TZ-3Y, Tosoh) in a 1:1 weight ratio of slurry to milling balls in a 200 g container until the powder was evenly coated with dispersant. Then, the monomers and diluent were added all together after which the slurry was mixed for 5 min at 2500 rpm. The photoinitiator was then added and the mixture was mixed for 3 min at 2500

rpm. Finally, the milling balls were removed, and the slurry was mixed in a low-vacuum setting (150 mbar) for 2 min at 2000 rpm in a 100 g container to remove air bubbles. An overview of the milling procedure is presented in Figure 2.

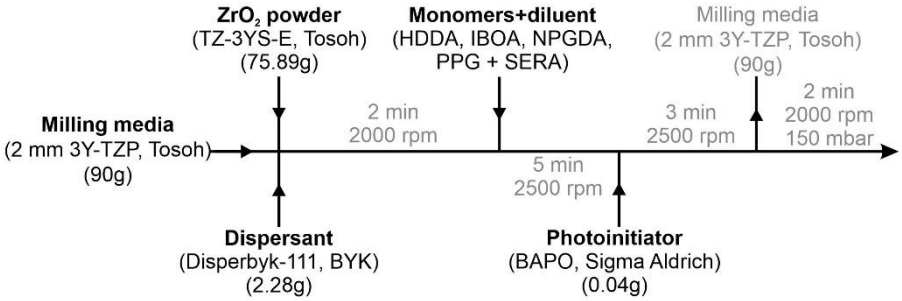

Figure 2. The mixing procedure of the ultimate HINP and 2SERA slurries used for ceramic object printing.

2.3 Slurry characterization

For sedimentation testing, a small amount of the acrylate slurries with varying dispersant content was diluted with the monomer and diluent mixture down to <1 vol% solid loading. 8 ml of this diluted slurry was loaded in a glass flask and photographed over the span of 8 weeks to determine the best dispersant type and amount. The viscosity of the loaded slurries was assessed using a flow sweep with a shear rate increasing stepwise from 0.1-200 s^{-1} using a rotational rheometer (MCR 702, Anton Paar, Graz, Austria) equipped with a stainless steel parallel plate setup (Ø25 mm). Measurements were performed at 20°C and a waiting time of 10 min was applied before starting the measurement. To ensure reproducibility, at least two repetitions were performed and a representative measurement was reported.

Curing tests were performed to determine the energy necessary to cure a certain thickness of slurry. A thin layer of slurry was dispensed on the printing foil and cured using the DLP of the 3D printer (Admaflex 130, Admatec, Alkmaar, The Netherlands) for a pre-set time and energy level. Uncured slurry was carefully removed by a soft paper cloth, after which the thickness of the cured ceramic slurry was measured using a digital calliper (0-25 mm IP65; Mitutoyo, Kawasaki, Kanagawa, Japan). The curing depth (C_d) was plotted as a function of the exposed energy (E) using Jacob's equation [31]:

$$C_d = S_d \ln \frac{E}{E_c}$$

where S_d is the sensitivity of the suspension representing the distance in the paste at which the light intensity is reduced by $1/e$ and E_c is the critical exposure energy, i.e. the energy threshold necessary for polymerization.

2.4 Digital light printing, debinding and sintering

Discs (Ø12 mm, 3 mm height after sintering), bending bars (3x4x30 mm^3 after sintering) and complex shapes were printed using a DLP printer (Admaflex 130, Admatec) with a wavelength of 405 nm. Before printing, a thin layer of uncured photocurable blend, consisting of acrylates and photoinitator, was coated onto the build platform to improve adhesion of the actual print. Next, the first two layers of every print were two high energy (270 mJ/cm^2) 30 µm layers of the ceramic resin covering the entire build platform to obtain an even base layer to print the ceramic prints on top and to facilitate print adhesion during printing and object removal after

printing. Slurries without and with 33 wt% of the different diluents summarized in Table 1 were then printed. The diluent wt% refers to the amount of diluent in the liquid slurry consisting of monomers and diluents. To determine the amount of diluent needed to have crack-free sintered ceramics, slurries made of the HIN composition (Table 1) with added diluent content varied from 10-33 wt% PPG-400 relative to the total monomer and diluent content were printed (as summarized in Table 3). All the slurry design tests discussed in sections 3.1-3.5 were printed using 30 µm layers and an exposure energy of 42 mJ/cm^2. Out of the final selected HINP composition (Table 2), samples were printed using a layer thickness of 10, 15, 20, 25 and 30 µm to determine the optimal layer thickness. A minimal curing depth was determined to ensure layer adhesion, which was determined to be at least 3 times the thickness of a single layer. A minimum curing depth of 75 µm was necessary to ensure good adhesion of the cured resin to the build platform and previously cured layers, regardless of the layer thickness. Energy doses of 30.4 mW/cm^2 were used for 15 µm layers and 42.0 mW/cm^2 for 30 µm layers respectively. After printing, the build platform was removed from the printer. The green body, which was still connected to the build platform, was manually cleaned using ethanol and a soft brush. The green bodies could carefully be removed manually from the building plate after cleaning because the base layer loosened from the build platform. Slight bending of the build platform could facilitate the removal of the printed part. A sharp box cutter was used to remove any remnants of support structures or base layer.

Table 3. Composition (wt%) of designed HIN-PPG slurries used to determine the optimum PPG-400 diluent content.

Slurry* →		**HIN-10PPG-400**	**HIN-15PPG-400**	**HIN-20PPG-400**	**HIN-25PPG-400**	**HIN-30PPG-400**	**HIN-33PPG-400**
Compounds (wt%) ↓							
Base Acrylates	**HDDA**	3.88	3.67	3.45	3.24	3.02	2.89
	IBOA	3.88	3.67	3.45	3.24	3.02	2.89
	NGPDA	3.88	3.67	3.45	3.24	3.02	2.89
Diluents	**PPG-400**	1.29	1.94	2.59	3.24	3.89	4.28
Photoinitiator	**BAPO**	0.04					
Dispersant	**Disperbyk-111**	2.53					
ZrO_2 powder	**TZ-3YS-E**	84.48			84.47		84.46

After cleaning, the green parts were thermally debound up to 525°C and pre-sintered at 1000°C for 1 h in a muffle furnace (laboratory furnace RHF 1200, Carbolite, Sheffield, United Kingdom) and sintered at 1450°C for 2 h in a HT 16/17 chamber furnace (Nabertherm, Lilienthal, Germany). The thermal cycles used are shown in Figure 3. To assist in defining the optimal debinding cycle, combined thermo-gravimetrical analysis and differential scanning calorimetry (TGA/DSC; SDT Q600, TA Instruments, Asse, Belgium) was performed at 10°C/min up to 800°C in air on as-printed disks of 2 mm diameter and 1 mm height.

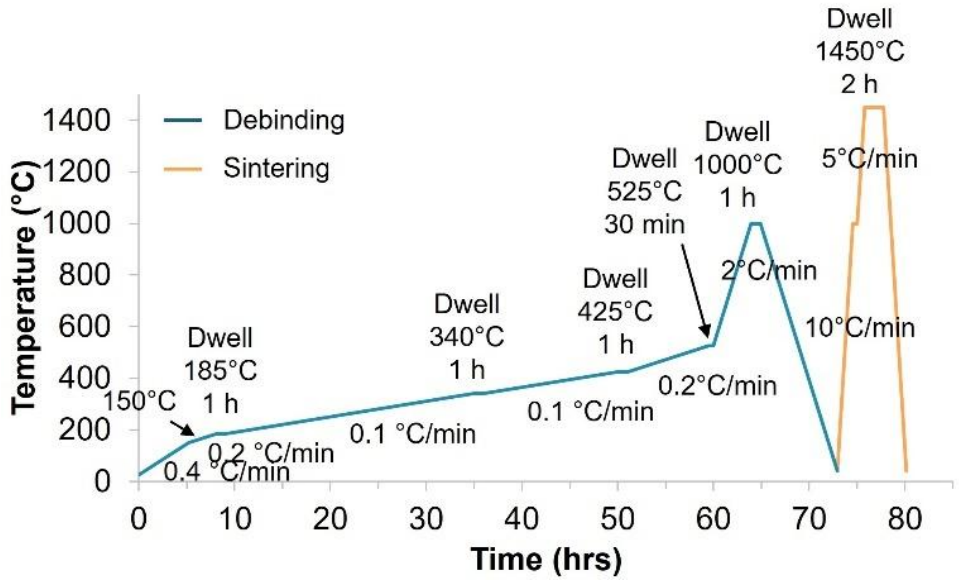

Figure 3. Thermal debinding (blue line) and sintering cycle (orange line) used for HINP and 2SERA slurry-based 3Y-TZP.

2.5 Characterization of as-printed and as-sintered ceramics

The density of all sintered ceramics was measured by the Archimedes' principle in ethanol. The relative density was calculated using 6.05 g/cm^3 as theoretical density for 3Y-TZP [32]. The trueness of the as-printed and shrinkage of the as-sintered ceramics was determined geometrically using a digital calliper (RS PRO 150 mm; RS Components, Corby, United Kingdom). Trueness is measured by calculating the degree of deviation between the as-printed green body samples in relation to the original CAD file, also referred to as polymerization shrinkage (Z) and overcuring (XY) in the text. Shrinkage is determined as the reduction in size of the sintered sample compared to the original CAD file.

The microstructure of the surface and cross-sections of both 3D printed and sintered ceramic discs was investigated using light microscopy (LM, Leica DM ILM, Leica Camera, Wetzlar, Germany) and scanning electron microscopy (SEM, XL30-FEG, FEI, Eindhoven, The Netherlands). Sintered samples were polished down to 1 µm using a silica suspension and coated with a 5 nm platinum layer.

The contact angle of distilled H_2O on green bodies of the HINP and 2SERA slurry compositions was measured using a drop and surface analyser (K100 SF tensiometer, Krüss, Hamburg, Germany). The green bodies were cleaned with ethanol after printing and dried in air for 24 h in a muffle furnace. A Laplace-Young fitting by the Pendant Drop software was used to calculate the contact angle of the H_2O droplet on the green body. The average of 5 separate measurements is reported.

The surface roughness of the sintered ceramics was measured in the building direction and on the top and bottom surfaces using a 3D Optical Profiler (S neox, Sensofar, Terrassa, Spain). The surface topography was acquired using a confocal objective of 20x, while the focus range varied over 120 µm using SensoSCAN (Sensofar) software. An area of 2.85 mm x 2.64 mm was scanned, by stitching smaller field of views with an overlap of 25%. The lateral resolution was 0.64 µm/pixel. The surface roughness was analysed using SensoMAP software (Sensofar). The samples were levelled, and a cut-off of 2.5 mm with a sample evaluation length of 2.5 mm was used [33,34]. The average surface roughness, S_a, of three different measurements on three different samples is reported [35,36]

The Young's modulus (E) was measured by the impulse excitation technique (IET; MK7, Grindosonic, Leuven, Belgium) on 10 sintered 4-point (4-pt) bending bars at room temperature. The flexural mode was used as vibration mode. Each bar was supported by a low stiffness triangular prism in the nodal points. The bar was excited by a 5 mm diameter stainless steel ball. The tests were performed according to ASTM E1876-01 [37].

The Vickers indentation hardness (H_V) and fracture toughness (K_{ind}) were measured (Model FV700, Future Tech, Kanagawa, Japan) with a load of 98 N for 15 s on sintered and mirror-polished discs. The indentation fracture resistance, K_{ind}, was obtained from the radial crack pattern generated by HV_{10} indentations and calculated according to the formula of Anstis *et al.* (1981) [38], using the E-modulus measured by IET. For repeatability, 10 indentations were made on two different samples and the average values and standard deviations are reported.

The green strength of bending bars (3x4x35 mm^3) with varying PPG-400 diluent content (0-33 wt% of the slurry matrix) in HIN slurries was determined using a 3-point (3-pt) bending setup with a span of 20 mm on a 4467 Tensile Tester (Instron, Norwood, MA, USA) and a crosshead speed of 0.5 mm/s. The 3-pt bending strength of as-sintered bending bars (3x4x30 mm^3) printed from the HINP slurry with a layer thickness of 15 µm, as well as 4-pt bending strength (inner and outer span of 10 and 20 mm) of as-sintered bending bars (3x4x30 mm^3) from HINP and 2SERA slurries printed with a layer thickness of 15 µm, were measured. The fracture surfaces were analysed by SEM to determine the origin of fracture.

3. Results and discussion

3.1 Dispersant selection

The influence of different dispersants and their contents on the viscosity of a 40 vol% ZrO_2-loaded HIN slurry (Table 1) at a shear rate of 1 s^{-1} is presented in Figure 4. All dispersants show a similar trend with a minimum viscosity at a certain dispersant concentration.

At a low dispersant concentration, not all ZrO_2 particles will be fully coated, which will cause the powder particles to agglomerate and increase the viscosity [39]. When the dispersant concentration is too high, the excess dispersant molecules will tend to entangle adhered dispersant and increase the viscosity. The addition of 5 wt% Disperbyk-180 (0.7 Pa·s) relative to the powder load resulted in the lowest viscosity, when compared to KD1, KD4 and KD24 and BYK-111. 3 wt% Disperbyk-111 (1.5 Pa·s) and 1 wt% KD1 (1.0 Pa·s) resulted in low viscosities similar to that of 5 wt% Disperbyk-180-dispersed slurry.

The results of the sedimentation test on diluted HIN-25 PPG-400 slurries with different amounts (1-8 wt% relative to the ZrO_2 content) and types of dispersants show that initially all dispersants allowed a homogeneous dispersion of the powder (see supplemental information, Figure S1). For both Disperbyk dispersants, the necessity of a minimum amount of 2 wt% dispersant can be noticed starting from day 10. After 20 days, most powder sedimented, whereas the diluted slurries containing >2 wt% dispersant still showed partial dispersion. KD24 stabilized 3Y-TZP fully sedimented after 20 days and even already at 10 days at low (≤0.5 wt%) and high (≥5 wt%) concentrations. KD1 and KD4 showed better results at lower concentrations around 1 wt%. These results show that the powder-dispersant bonding after speedmixing might not be as strong as for longer premixing, as reported by Sun et al. (2019) [40], since they observed no sedimentation up to 20 days using a non-specified type of Disperbyk dispersant.

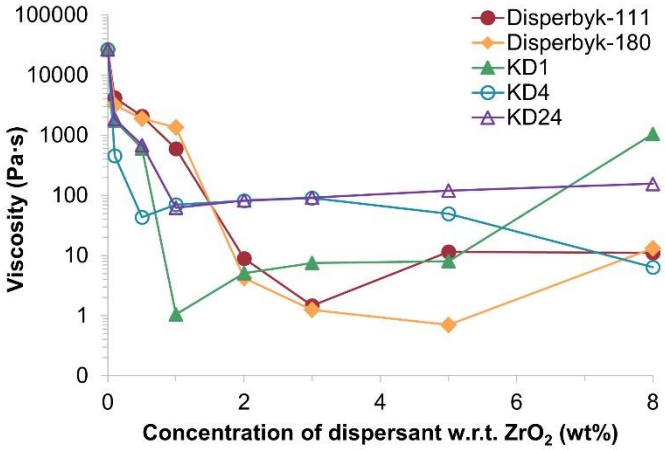

Figure 4. Viscosity (at a shear rate of 1 s^{-1}) of HIN-25PPG-400 slurries containing 0.1-8 wt% (relative to the ZrO_2 powder load of 40 vol%) of Disperbyk-111, Disperbyk-180, KD1, KD4 and KD24 dispersants.

3.2 Influence of diluent or reactive monomer-based diluent addition

This section investigates the addition of diluents to HIN-slurry. The composition of the investigated slurries is given in Table 1, and are referred to as HIN-X extra, with x being the wt% (relative to the monomer and diluent content in the slurry) of the additional reactive monomer-based diluent (TPGDA or PPA) or non-reactive diluent (PEG-200, PPG-400 or PPG-1000).

The influence of the diluent on the TGA/DSC curves of a printed disk is shown in Figure 5, and the thermal decomposition strongly depends on the slurry composition, as illustrated in Figure 6. The HIN slurry containing only reactive monomers and 3 wt% Disperbyk-111 relative to the powder content has three clearly distinguishable exothermal peaks (marked as 1, 2 and 3) in the 300-500°C region of the DSC curve in Figure 5A, which are linked to the degradation of the cured polymers and the evaporation of gases formed. All printed green bodies showed a weight loss starting from 150°C onwards, but the diluent-containing prints (PEG-200, PPG-400, PPG-1000) had a higher decomposition rate at lower temperature. This was observed by the faster mass loss at lower temperatures for the diluent-containing prints. They also have a fourth exothermal peak (marked as 4D) around 200-250°C, indicating the oxidation of diluents during thermal decomposition prior to the decomposition of the crosslinked monomers. The intensity of the exothermal peak 4D increased with increasing PPG molecular weight. The prints with only reactive monomers (observed in Figure 5A-B) have a small exothermal peak around 200°C, which is indicated by *. This could be caused by a small amount of non-polymerized monomer burning out. The burning out of the PEG and PPG diluents at lower temperature can create a porous structure, improving the thermal debinding of the polymer matrix at higher temperatures by allowing air and formed gases to more easily diffuse through the partially debound print [41]. The addition of TPGDA and PPA monomers only cause a change in the relative 1/2/3 peak intensities, without any change in the debinding characteristics in the lower temperature window with respect to the HIN slurry.

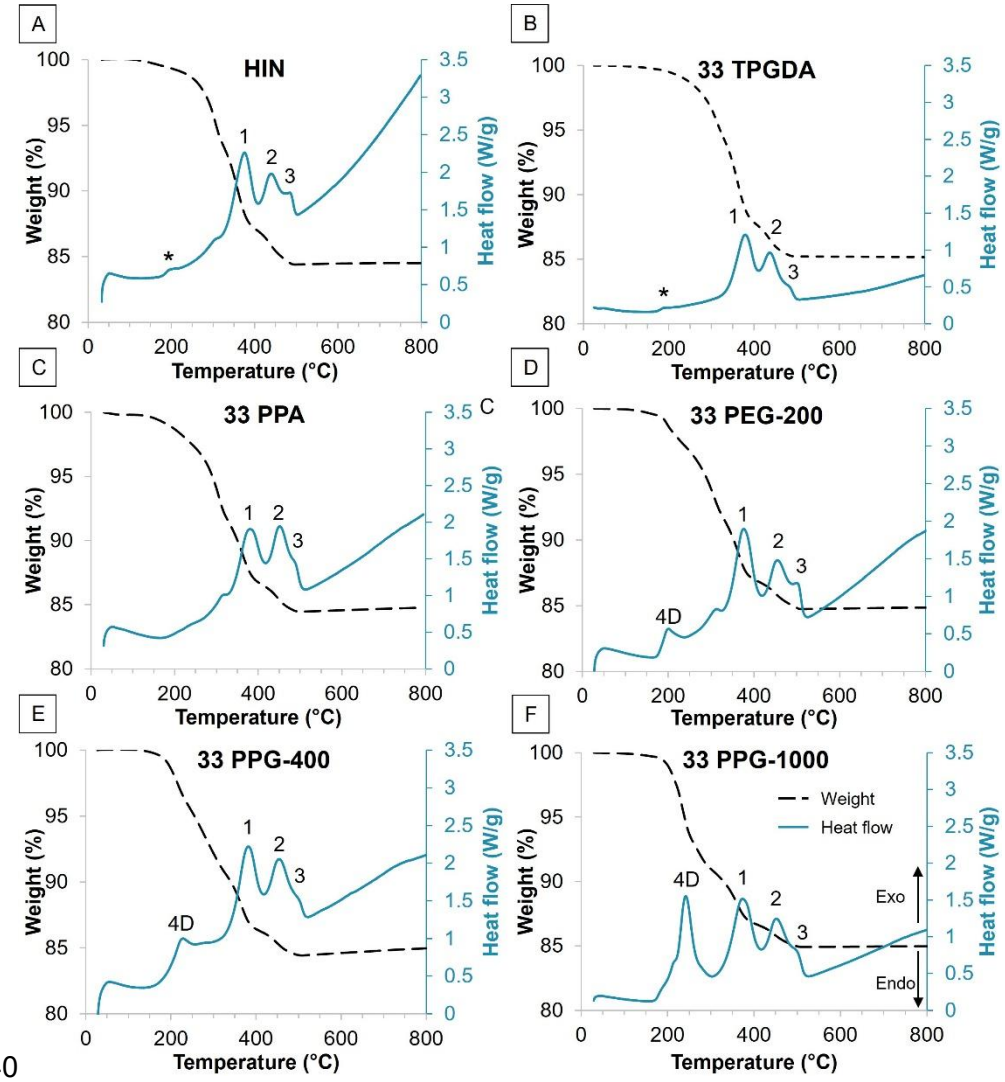

Figure 5. TGA/DSC of as-printed ceramics using 48 vol% ZrO_2 based various slurries: (A) HIN, (B) HIN-33TPGDA, (C) HIN-33PPA, (D) HIN-33PEG-200, (E) HIN-33PPG-400 and (F) HIN-33PPG-1000. The slurry composition is shown in Table 1.

As shown in Figure 6, it was not possible to obtain crack-free thermally debound and sintered 3Y-TZP ceramics when using only the 3 base reactive monomers (HIN slurry) without any diluents. Adding reactive monomer-based diluents (TPGDA or PPA) did not improve the microstructure after thermal debinding and sintering (Figure 6B and C). The sintered PEG-200 containing print showed small cracks, possibly due to swelling by water absorption during the cleaning step, as shown in Figure 6D. It was however possible to obtain near-fully dense crack-free ZrO_2 ceramics using 33 wt% of the PPG-400 and PPG-1000 diluents in the matrix (Figure 6E and F). During debinding, cracks perpendicular to the printed layers are formed due to a high binder content, as well as delamination cracks along the layer interfaces. Both cracks are triggered by gas formation during the debinding process. During sintering, the cracks along the layers are prone to propagate, resulting in complete part delamination [42]. The shorter perpendicular cracks and longer delamination cracks are observed in the prints made of only reactive monomers in Figure 6. It can be concluded that the non-reactive PPG diluent-containing slurries led to successfully debound and near fully dense sintered 3Y-TZP ceramics with a crack-free bulk. Typical edge defects however could still be observed in all printed and sintered ceramics. This will be further dealt with in section 3.6.

All 48 vol% 3Y-TZP-loaded slurries led to nearly fully dense ceramics (Table 4). All 48 vol% resins were printed using a layer thickness of 30 µm and the same energy dose of 42 mJ/cm^2. The addition of non-reactive diluents decreased the sintering shrinkage in the building (Z) direction (Table 4), in agreement with literature reports on SLA of alumina [41]. The trueness of the parts containing non-reactive PEG and PPG diluent slightly improved in the Z direction because the monomer content was even lower and less shrinkage occurred. This is however not the case for HIN-33PPG-1000. The high viscosity of this slurry (Figure 7) might have caused issues with the dispensing of the resin during printing and/or with the coating of the print resulting in more shrinkage and inaccuracies [43]. Finding the correct printing parameters will have the most significant impact on the trueness in the XY direction. Excessive curing energy will cause more scattering in the resin and an excess of material cured. A higher energy will also have an impact on the Z-direction trueness since curing the resin more intensively might make it shrink more in the Z direction.

Table 4. Trueness of the printed part and density and sintering shrinkage of sintered ceramics printed from various slurries with 48 vol % solid loading.

Slurry	XY Trueness (%)	Z Trueness (%)	Density (g/cm^3)	XY Shrinkage (%)	Z Shrinkage (%)
HIN 48 vol% 3Y-TZP	0.1±0.5	-1.1±0.2	6.04±0.01	20.2±0.1	21.3±3.1
HIN-33TPGDA	3.6±0.1	-2.6±1.4	6.00±0.01	17.2±0.2	21.5±0.8
HIN-33PEG-200	0.7±0.5	-1.0±0.7	6.01±0.01	17.9±0.1	19.0±0.8
HIN-33PPG-400	2.5±0.0	-0.7±0.1	6.03±0.01	21.8±0.2	20.4±0.2
HIN-33PPG-1000	0.8±0.9	-3.1±3.0	6.03±0.02	20.7±0.2	19.1±1.1
HIN-33PPA	1.2±0.2	-2.9±1.5	6.03±0.02	22.1±0.2	21.4±1.6

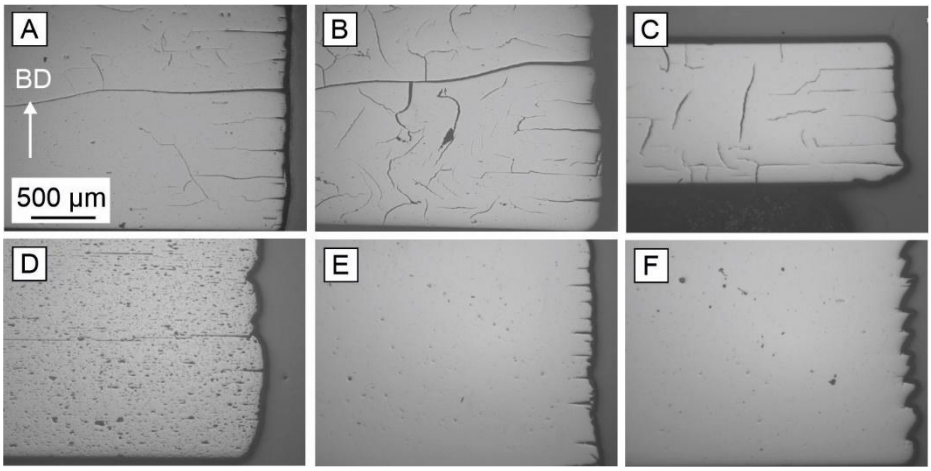

Figure 6. Optical micrographs of cross-sectioned sintered ceramics printed with different slurries: (A) HIN 48 vol% ZrO_2, (B) HIN-33 TPGDA, (C) HIN-33PPA, (D) HIN-33PEG-200, (E) HIN-33PPG-400 and (F) HIN-33PPG-1000. The arrow in A represents the build direction (BD) and all images have the same scale as shown in A.

The viscosity of the diluent has an influence on the viscosity of the slurry (Figure 7). The higher molecular weight and concomitant higher viscosity of PPG-1000 and PPG-2000 significantly increased the viscosity of the slurry, as shown in Figure 7A. The addition of 10 wt% PPG-2000 increased the viscosity beyond the maximum of 10 Pa·s for dispensing and therefore there were no TGA/DSC results included in Figure 4. The 10 wt% PPG-1000 sample is insufficient to obtain crack-free debound and sintered ceramics, and adding more PPG-1000 resulted in a resin that did not remain below the 10 Pa·s viscosity limit (Figure S3 in the supplemental

information). The viscosity of the slurry clearly increased with increasing diluent molecular weight. The influence of PPG-400 on the viscosity was much smaller, as illustrated in Figure 7B, with a slightly increasing viscosity as a function of diluent content.

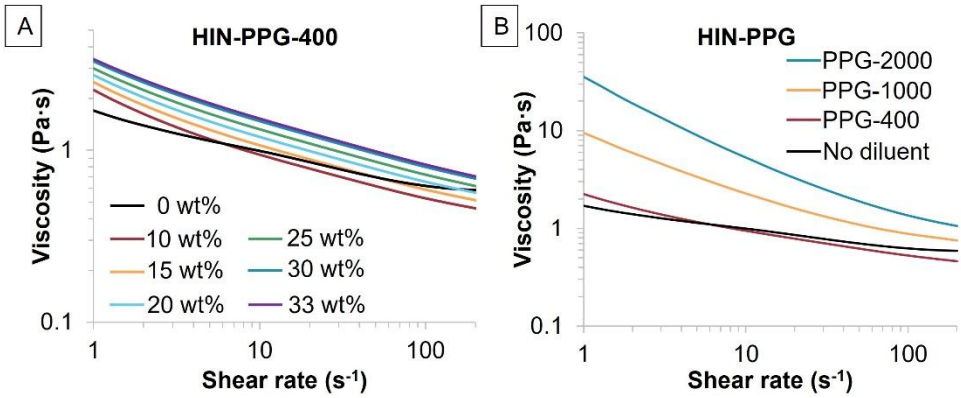

Figure 7. Flow sweeps of 40 vol% 3Y-TZP loaded slurries containing (A) 0-33 wt% PPG-400, and (B) no diluent, compared to 10 wt% PPG-400, PPG-1000, and PPG-2000.

3.3 Influence of PPG-400 diluent content

Due to the increasing viscosity with increasing molecular weight of the PPG, PPG-400 was chosen as the more appropriate diluent. To determine the minimum amount of PPG-400 necessary to obtain crack-free bending bars of desired size (≥ 4 mm thick after sintering), slurries containing 48 vol% 3Y-TZP and equal amounts of HDDA, IBOA and NGPDA and 10-33 wt% of PPG-400 relative to the monomer and diluent content (see Table 3), were printed, thermally debound and sintered. The results are shown in Figure 8, revealing that minimum 25 wt% of PPG-400 (relative to the monomer content of the slurry) was necessary to obtain crack-free ceramics. A content below 25 wt% PPG-400 resulted in delaminated prints, especially at the edges, so 25 wt% PPG-400 was found to be the optimal concentration.

Since the non-reactive PPG-400 diluent does not UV-cure, the flexural strength of the printed ceramic green bodies will decrease with increasing PPG-400 content, as shown in Figure 9A. A linear decrease in green bending strength with increasing diluent content was measured, due to the decreased photopolymerized binder content. The flexibility however increased with increasing diluent content, as shown in Figure 9B. A higher flexibility combined with lower green strength can result in the parts being separated from the build platform during printing, especially during the upward movement of the build platform after curing a layer. A commonly accepted minimum strength allowing green machining of ceramic compacts is 20 MPa. The selected slurry containing 25 wt% PPG only has a strength of 11.3 MPa. Although DLP-printed ceramics normally do not need green machining, they should undergo post-processing procedures such as removal from the build platform, support removal and cleaning of uncured slurry. These post-processing procedures are often performed manually and are often dependent on the applied printing technology. More research is needed to define a minimum green body strength necessary to facilitate these post-processing steps [44]. A lower green strength will create more defects that can be introduced, so it is in our best interest to keep the PPG content as low as possible.

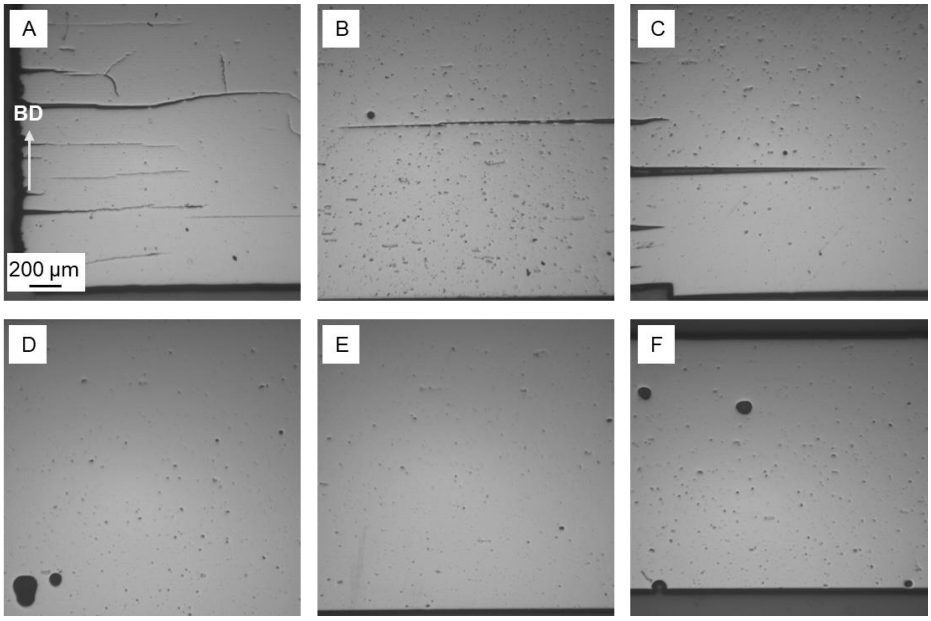

Figure 8. Optical micrographs of sintered ceramics from slurries containing (A) 10, (B) 15, (C) 20, (D) 25, (E) 30, and (F) 33 wt% PPG-400. The arrow in A represents the build direction and the scale is valid for all images.

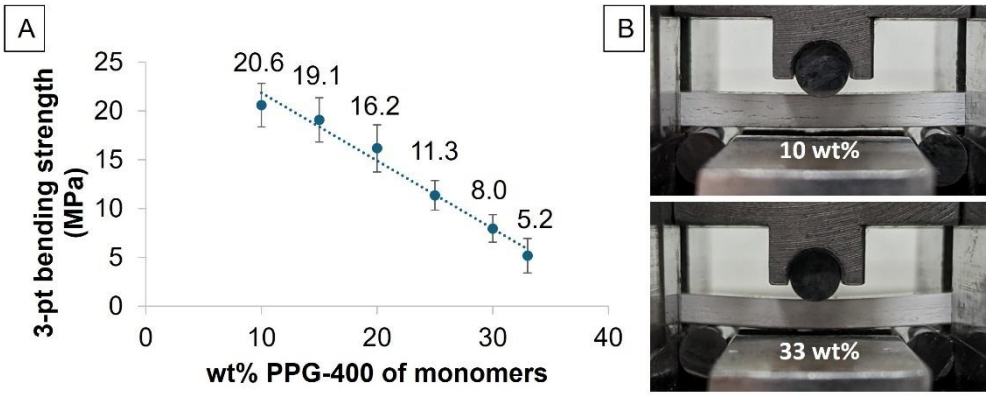

Figure 9. (A) Green strength of printed ceramics with varying PPG-400 content. (B) Visualization of increased flexibility with increasing PPG-400 content.

3.4 Solid loading

Since the addition of dispersants KD1, Disperbyk-111 and Disperbyk-180 gave similar rheological results, depending on the dispersant content, their effect on the viscosity was investigated in more detail at different powder loads, as summarized in Figure 10. The viscosity of the slurry increased with increasing powder load and a shear-thinning behaviour was observed for all dispersant types. Disperbyk-180 showed the lowest viscosity and allowed a solid load of 48 vol% with a viscosity that remained below the 10 Pa·s viscosity limit at a shear rate above 1 s^{-1} [45]. The final solid loading for the printing paste was chosen to be 48 vol%, as shown in Table 2, and was used from this point in this work.

Based on the viscosity measurements, slurries containing 48 vol% ZrO_2 were proof-printed using 5 wt% Disperbyk-180, 3 wt% Disperbyk-111 or 1 wt% KD1 relative to the solid powder load. The 5 wt% Disperbyk-180 containing slurry, however, cured too softly and the layers did not adhere well enough, leading to inaccurate and broken prints. The higher amount of Disperbyk-180 dispersant compared to the 3 wt% Disperbyk-111 or 1 wt% KD1 slurries led to

a lower monomer content in the slurry, decreasing the strength of the prints. It was possible to successfully print the slurries containing 48 vol% ZrO_2 with 3 wt% Disperbyk-111 or 1 wt% KD1 dispersant. Since the 3 wt% Disperbyk-111 slurry had the lowest viscosity of both slurries (see Figure 10), 3 wt% Disperbyk-111 was selected as most promising printing slurry. The lower viscosity will improve the quality of the prints through lower separation forces and better dispensing properties [45,46]

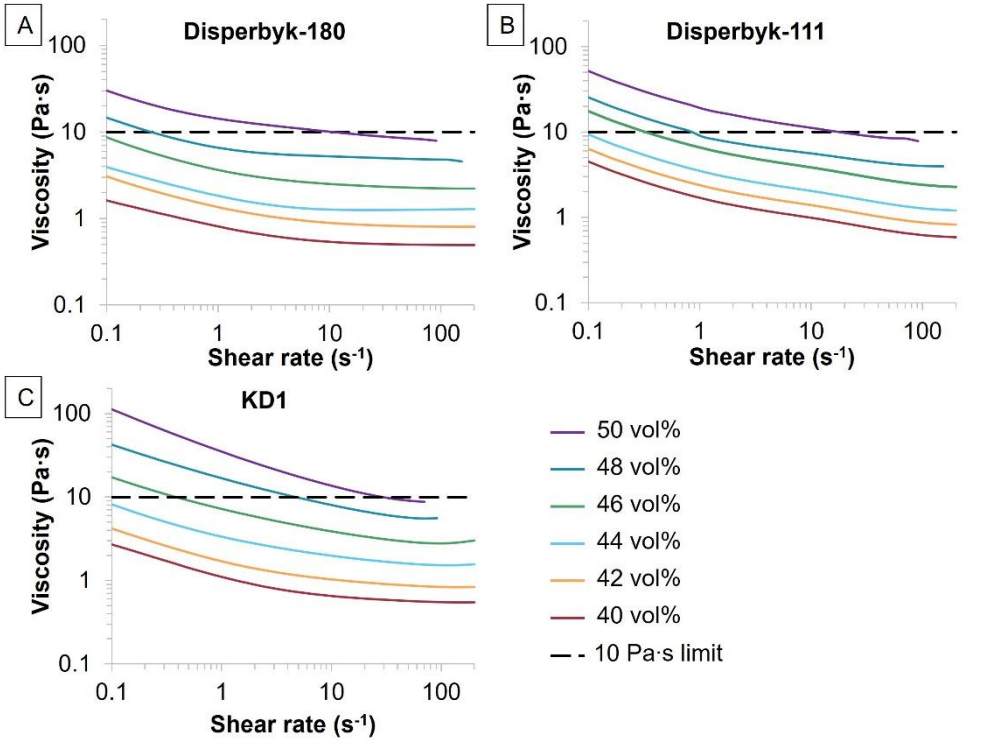

Figure 10. Viscosity of HIN-25PPG-400 slurries containing (A) 5 wt% Disperbyk-180, (B) 3 wt% Disperbyk-111, and (C) 1 wt% KD1 with varying solid loads of 3Y-TZP powder (40-50 vol%). The black dashed line indicates the reported viscosity limit of 10 Pa·s for dispensing.

3.5 Photoinitiator content and curing behaviour

The curing curves for HIN-25PPG-400 slurries with 48 vol% ZrO_2 and 3 wt% Disperbyk-111 dispersant, containing 0.33 and 1 wt% of BAPO (relative to the monomers), are plotted in Figure 11A. The curing depth at the same energy dose actually decreased with increasing BAPO content, implying there is an optimum amount of photoinitiator to be added to the slurry [47]. Not only a higher energy dose was necessary for slurries containing 1 wt% BAPO, but also extensive overcuring in the in-plane direction was obtained (Figure 11B-C). The print shown in Figure 11B was cured at 91 mJ/cm^2, resulting in a curing depth of 75 µm (2.5x layer thickness), whereas the print in Figure 11C was cured with a smaller energy dose of 73 mJ/cm^2 resulting in a curing depth of 60 µm (2x layer thickness). Figure 11B-C shows that larger and smaller portions of the part did not adhere well to the print due to insufficient adhesion and curing of the layers. Given that the in-plane overcuring increased with increasing energy dose, it was concluded that 1 wt% BAPO did not allow accurate printing of ceramic parts with this slurry. A higher photoinitiator concentration initially increases the rate of polymerization, which can translate to a greater curing depth. However, photoinitiators also absorb UV light. As the concentration increases, more light is absorbed near the surface of the slurry, reducing the amount of light that can penetrate deeper into the material [47]. The high content of zirconia powder combined with a higher absorbance of light at the surface of the slurry in case of a too high photoinitiator content, will result in more light scattering and more in-plane overcuring.

When decreasing the photoinitiator content to 0.33 wt% (relative to the monomer content), it was possible to obtain an accurate design without extensive overcuring in the XY-plane with a exposure energy of 42 mJ/cm^2 resulting in a curing depth of 3 layers (90 µm) as shown in Figure 11D. A lower energy dose (23 mJ/cm^2) with a lower curing depth of only 2 layers (60 µm) did not ensure good adhesion of the cured layers. A BAPO content of 0.33 wt% relative to the monomer content was therefore deemed optimal for the HIN-25PPG-400 slurry. This is referred to as the HINP slurry (Table 2), containing a 1:1:1:1 ratio of HDDA, IBOA, NGPDA and PPG-40, 48 vol% ZrO_2 powder, 3 wt% Disperbyk-111 (relative to the ZrO_2 content) and 0.33 wt% BAPO (relative to the monomer content). The critical exposure energy E_c is 6.8 mJ/cm^2 and the sensitivity S_d is 49.5 µm for the final HINP slurry. This slurry allowed printing with curing depths of 90 µm, guaranteeing a good layer adhesion.

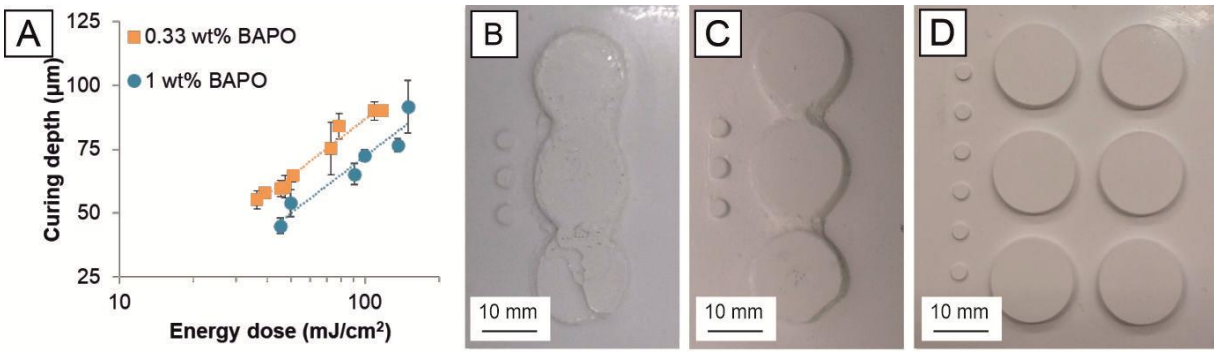

Figure 11. Working curves of slurries with 0.33 and 1 wt% BAPO (A) and printed parts with 1 wt% BAPO at different exposure energies (B-C) and 0.33 wt% BAPO (D).

The TGA/DSC curve of the HINP slurry, shown in Figure S2 in the supplementary information, is similar to that of the HIN-33PPG-400 slurry shown in Figure 5E, but with a relatively smaller exothermal peak around 250°C due to the lower PPG-400 content. At 525°C, both the heat flow and weight loss and the total weight loss of the TGA measurement is in very good agreement with the 15.53 wt% organic material in the slurry, implying all binder is removed around 525°C. Based on the TGA/DSC curve, a debinding cycle (see Figure 3) with a heating rate of 0.4°C/min is applied up to 150°C. Above 150°C, a slower heating rate of 0.1-0.2°C/min is applied until all binder is burned out. A 1 h dwell period was applied at 185°C, 340°C and 425°C. Above 525°C, a heating rate of 2°C/min was applied up to 1000°C to shortly pre-sinter the sample before cooling down to room temperature. Since debinding and sintering was done in different furnaces to ensure accurate temperature and heating rate control, the sample was pre-sintered at 1000°C after debinding to provide enough green strength by neck formation allowing safe manipulation.

3.6 Influence of a surface energy reducing agent (SERA)

In order to try to eliminate the typical edge delamination initiating defects, as illustrated in Figure 6, the addition of an additive was explored to reduce the surface tension of the HINP slurry to improve substrate wetting and to decrease the separation forces at the interface of the print and the polypropylene dispensing foil during DLP. The influence of varying amounts of BYK-UV 3500 (BYK), a silicone-containing surface energy reducing agent (SERA), was assessed. The reported wt% of SERA was relative to the overall monomer and diluent content. Figure 12 shows that the printed green bodies become more hydrophilic upon adding the SERA surfactant, since the water contact angle (θ) decreased from 36.7° for the HINP slurry to 16.3° and 13.0° for 2 wt% and 5 wt% SERA content slurries, respectively. No significant difference was obtained between 2 wt% and 5 wt% SERA addition. The biaxially oriented polypropylene DLP foil was also hydrophilic, since $\theta < 90°$, but was less hydrophilic than the

slurry prints. The increased hydrophilic character of the prints will allow better wetting between the print and a fresh layer of slurry. By making the slurry more hydrophilic, the adhesion with the foil was reduced and the adhesion to the already printed material improved.

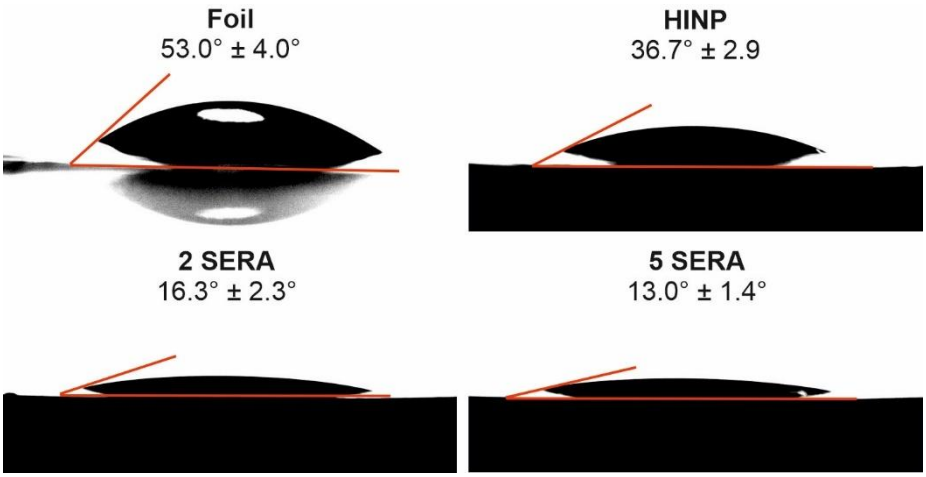

Figure 12. Water droplet contact angle measurements on the dispensing foil and printed green bodies containing no (HINP), 2 wt% (2 SERA) or 5 wt% (5 SERA) BYK-UV 3500.

The change in microstructure upon addition of SERA is shown in Figure 13. For a 30 µm layer thickness print, the common protrusions observed at the edge of the prints, change into smaller and straighter edge defects upon addition of 2 wt% SERA. 5 wt% SERA addition did not show a further improvement in the microstructure. The refractive index of SERA is 1.443, which is comparable to that of the monomers used, indicating that the edge surface roughness and concomitant initiation of delamination is not only caused by overcuring due to the high refractive index of ZrO_2, but also by the wetting of the slurry and the green print.

While the as-printed and as-sintered ceramic showed smaller side protrusions, i.e. a smoother edge surface, by adding 2 wt% SERA, the micro-cracks present on the side of the green body had the tendency to propagate during debinding and sintering and resulted in a similar edge notching defect with a similar crack length as without SERA addition.

Although the SERA addition did decrease the surface tension and improve the edge microstructure of the prints, further tailoring was needed. Although the study by Alamdari et al. [48] indicated that the SERA additive allowed the separation from glass plates to be improved, it would be interesting to investigate surface additives that could improve the wetting behaviour and decrease the separation forces from a biaxially oriented polypropylene foil. The choice of diluent in the slurry can have a significant impact on debindability as discussed in section 3.2, but it can also impact the green body strength and concomitantly the edge defects observed [49]. Postcuring the green body after printing could cure the acrylates which may not have been fully reacted during printing, improving green body strength and impact debinding [50]. A different, less aggressive cleaning solution and alternative cleaning solutions like airbrushing could also decrease the surface roughness and edge defects [51]. Apart from improving the slurry composition and the printing parameters, debinding under inert atmosphere might also decrease the presence of these observed defects [52,53]. Future research will be focused on these possible solutions.

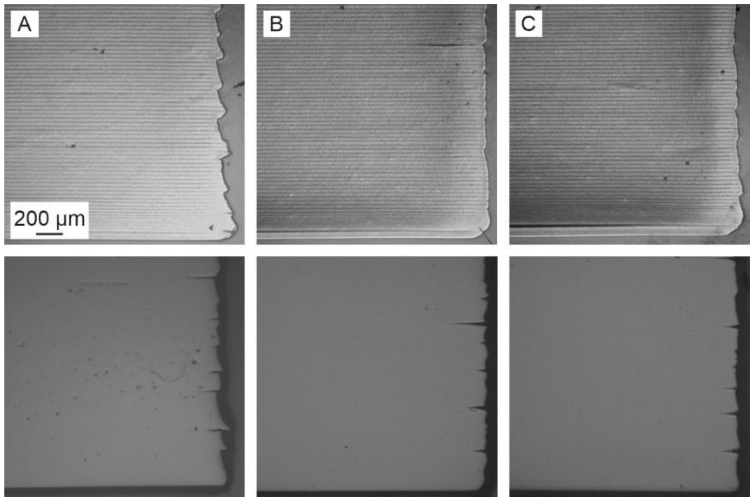

Figure 13. Optical micrographs of HINP slurry-based 3D printed (top) and sintered (bottom) ceramics containing (A) no SERA, (B) 2 wt% SERA, and (C) 5 wt% SERA. The scale in A is valid for all images.

3.7 Mechanical properties

The density, Vickers hardness, indentation fracture resistance, Young's modulus, average and characteristic 4-pt bending strength and Weibull modulus of the HINP and 2SERA (see Table 2) slurry-based sintered bending bars are reported in Table 5. The samples were printed in 15 µm layers and an energy dose of 30.4 mJ/cm^2 with a curing depth of 5 layers (75 µm).

Near fully dense 3Y-TZP ceramics could be obtained with the developed photopolymeric slurries. A density of 99.8±0.2 and 99.8±0.1 %TD was obtained for the HINP and 2SERA slurry-based ceramics respectively. Both Vickers hardness and fracture toughness are comparable to what has been reported for 3Y-TZP sintered at 1450°C for 2 h [54,55]. There is no anisotropy in fracture toughness due to the high density and there is no visible layerwise build-up in the bulk of the sintered ceramics. The Young's modulus is similar for both compositions and close to 210 GPa, a typical value reported in literature for 3Y-TZP.

The Weibull plots of the sintered 4-pt bending bars printed and loaded in the X-direction for both compositions are presented in Figure 14. The average and characteristic bending strength of both compositions are the same, and the Weibull moduli are also similar (Table 5). Since the addition of SERA mainly influenced the edge quality of the printed samples, and edge defects were still present in the final sintered ceramics, the effect of SERA addition is not reflected in the Weibull plot of X direction printed and tested bending bars.

Table 5. Density, Vickers hardness H_V, indentation fracture resistance K_{IC}, Young's modulus E, average σ_m and characteristic σ_0 4-pt bending strength and Weibull modulus m of the HINP and 2SERA slurry-based sintered ceramics.

Slurry		Density (g/cm^3)	H_V (GPa)	K_{IC} (MPa m$^{1/2}$)	E (GPa)	σ_m (MPa)	σ_0 (MPa)	m
HINP	**0°**	6.04±0.01	12.8±0.2	3.9±0.1	207±2	521±83	556	6.8
	90°		12.9±0.2	3.8±0.1	-	-	-	-
2SERA	**0°**	6.04±0.00	12.9±0.1	4.0±0.1	205±1	526±77	559	7.8
	90°		12.8±0.2	3.9±0.1	-	-	-	-

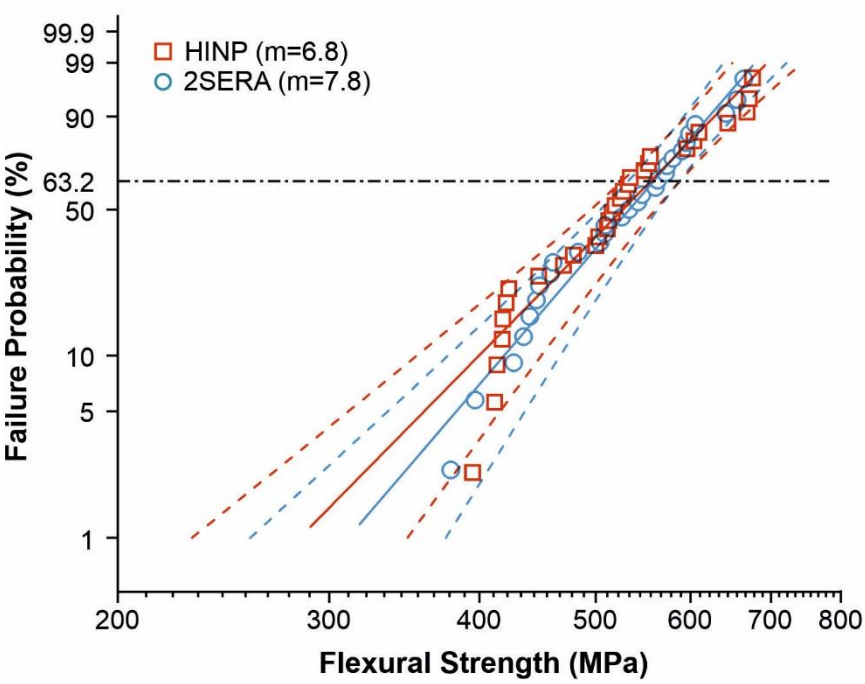

Figure 14. As-sintered 4-pt bending strength Weibull plot of HINP and 2SERA slurry-based materials.

The modest bending strength obtained for optimized HINP and 2SERA in this work was due to the residual defects that were observed inside the ceramics, as illustrated in Figure 15. The fracture origins in the higher-strength sintered prints were small surface defects or single pores (Figure 15A) or small surface cracks possibly induced by manual handling during post-processing (Figure 15B). Multiple smaller edge defects like agglomerates and surface cracks can lead to multiple fracture mirrors starting from the tensile side, known as zipper cracks (Figure 15C). The lower-strength samples had larger defects at the fracture origins like surface defects and pore channels (Figure 15D-E). The typical printing edge defects (Figure 13), i.e. the partial delamination of printed layers at the side of the part did not seem to be the strength-limiting factors, but the surface cracks along the layers did tend to propagate during fracture as indicated by the dashed white arrow in Figure 15C. The edge defect might have grown during loading and interacted with the crack propagation front resulting in the Wallner lines above and below the edge defect. No clear distinction between the types and sizes of the defects at the fracture origins could be made between HINP and 2SERA slurry-based ceramics. Both mainly had pores due to air bubbles in the slurries, agglomerates and edge cracks through print stresses or handling during post-processing as their main failure modes. The Weibull plots also indicate that both slurry-based 3Y-TZPs had similar defect distributions. Typical reported defects in literature for VP-produced ZrO_2 ceramics are pores due to air bubbles in the slurries, agglomerates, delamination, cracks due to differential shrinkage or insufficient layer bonding, and post-processing induced damage [21–24,56,57]. In addition, it is noteworthy that the average 4-pt bending strength (521±83 MPa) of the bending bars made from the HINP slurry (Table 5 and Figure 14) was significantly lower than the 3-pt bending strength (730±64 MPa) (Table 6). Although the sample dimensions were the same for both the 4-pt and 3-pt bending strength, the sensitivity to processing defects is higher for 4-pt bending bars due to the difference in maximum stress distribution during flexural loading and the larger effectively loaded volume. Given the amount of processing defects that were

observed in the printed bending bars, the resulting lower strength for 4-pt bending bars is a more accurate representation of the performance of the ceramics.

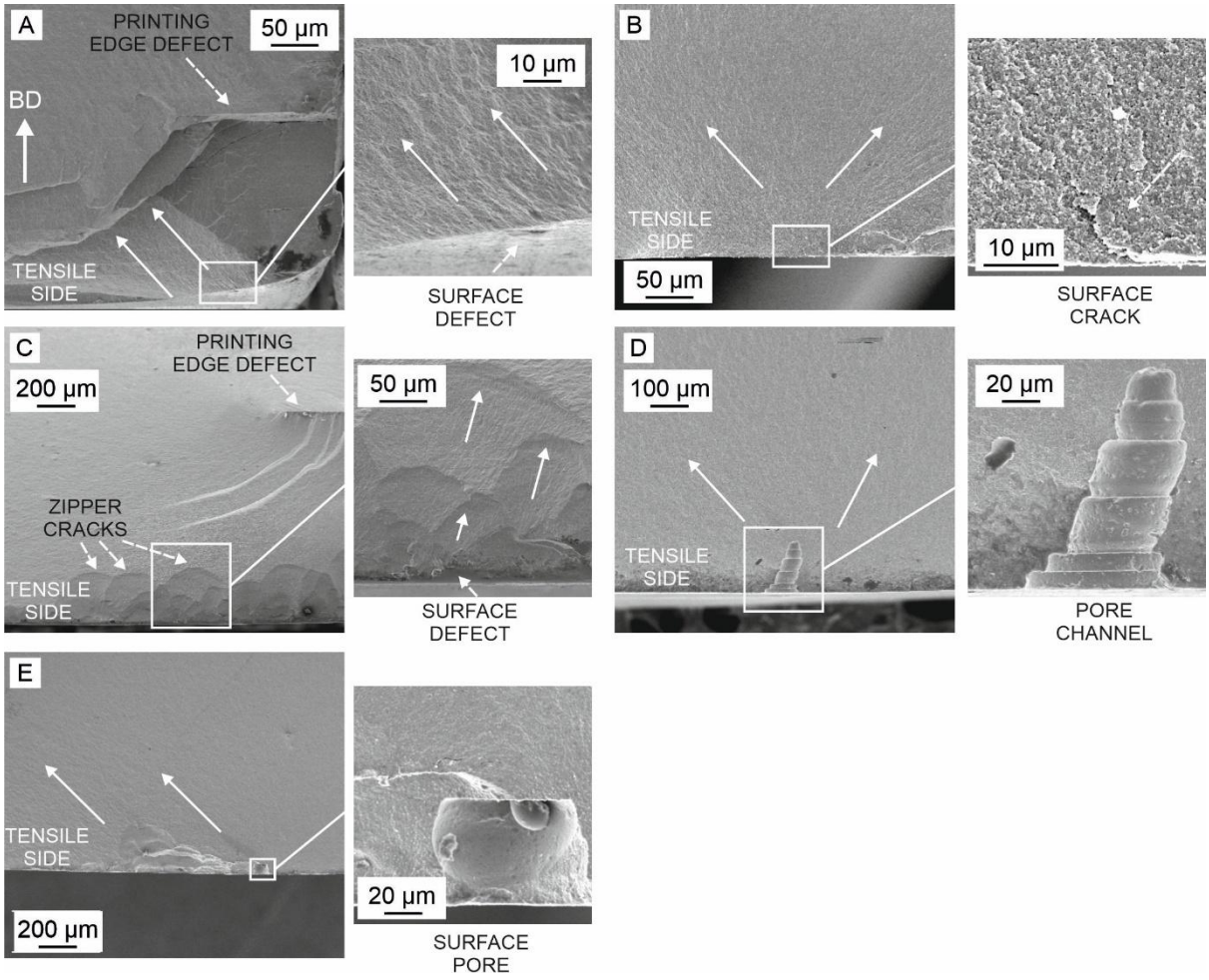

Figure 15. Fracture surfaces of HINP and 2SERA slurry-based 4-pt bending bars build in the X-direction. BD: building direction. The crack-propagation direction is indicated by white arrows. The white squares indicate the fracture origin that is enlarged. The enlarged version of every fracture origin with a description is given for every figure and dashed arrows indicate the position. Other defects like printing edge defects are also indicated by dashed white arrows.

Over the years, a lot of progress in mechanical performance has been made for SLA/DLP 3Y-TZP, as summarized in Table 6. Calculated converted 4-pt bending strength data was also reported in Table 6 (see section S2 in the supplementary document for the procedure of converting 4-pt strength). The reported 3Y-TZP strength data were obtained on a wide range of sample dimensions, and either tested in a 3-pt or 4-pt bending setup or even biaxially (see Table 6). Most studies used a smaller thickness for the bending specimen, which will lead to a smaller volume and a higher strength. However, a small specimen size will affect the reliability and the measured strength, especially in a technique like LCM that still produces ceramics containing many types of defects [58]. Zhai *et al.* (2024) [59] reported higher flexural strengths but polished the printed bending bars which has been reported to increase the strength [60]. The flexural strength of the printed materials in this work is still substandard compared to conventional manufacturing due to the presence of defects introduced by printing and manual handling during post-processing afterwards. The 3-pt flexural strength of the printed materials in this work is in line with the reported strengths in literature. Only the studies by Lu *et al.* [24], Sun *et al.* (2021) [16] and Li *et al.* (2022) [61] reported significantly higher

strengths. Sun *et al.* (2021) [16] reported that very few defects, except for a few pores were found in the printed and sintered 3-pt bending bars. Both studies of Lu *et al.* [24] and Sun *et al.* (2021) [16] used a higher solid load of 58 vol%, which results in less sintering shrinkage and improved mechanical properties The result by Sun et al. (2021) [16] showed that it is possible to obtain ceramics with a similar performance (1042±75 MPa) as conventionally manufactured 3Y-TZP. They underline the importance of finding the right printing direction, where in this study the X-direction was investigated. The 3Y-TZP slurry of Li *et al*. (2022) [61] only had a solid load of 44 vol% but they reported a very high bending strength, while using a limited set of flexural bending bars tested.

*Table 6. Overview of reported bending strengths of DLP/SLA 3Y-TZP. The nomenclature for the printing orientation and resulting loading orientation are shown in Figure S4 in the supplemental info. * in the references indicates the results of this work, σ_m and σ_0 are the average and characteristic 4-pt bending strength respectively, and m indicates the Weibull modulus. Converted σ_{m4pt} is based on volume difference between 3-pt and 4-pt strength test when Weibull modulus was reported, and for the values of this work they were physically measured.*

Tech-nique	Test	σ_m (MPa)	σ_0 (MPa)	m	Specimen number tested	Specimen size (mm^3)	Printing orienta-tion	Converted σ_{m4pt} (MPa)	Ref
DLP	3-pt	675±32	-	-	10	-	X	-	[62]
DLP	3-pt	307±6	-	8.8	10	36x4x3	X	265	[63]
DLP	3-pt	580	-	8.8	10	35x4x3	X	479	[64]
DLP	3-pt	1013±126	1066	9.3	9.3	22x4x1.4	X	841	[24]
DLP	biaxial	737±100	778	8.7	30	Ø21.6x1.2	X	-	[24]
DLP	3-pt	-	851	6.4	26	25x2.5x2.2	X	664	[23]
DLP	3-pt	-	939	11.2	26	25x2.5x2.2	Z	671	[23]
SLA	biaxial	-	1071	16.3	15	12x12x1.2	X	-	[25]
DLP	biaxial	-	935	8.1	15	12x12x1.2	Z	-	[25]
SLA	3-pt	320±41	338	8.2	6	25x4x1.2	X	234	[65]
DLP	3-pt	816±100	-	-	10	25x2x3	X	-	[66]
DLP	3-pt	855±113	-	-	-	25x5x2	Z	-	[67]
DLP	3-pt	1042±75	1076	16.4	40	45x4x3	X	949	[16]
SLA	3-pt	866±149	929	6.4	15	30x4x3	X	709	[67]
SLA	3-pt	1117±122	-	-	-	24x4x2	-	-	[60]
DLP	3-pt	122±5	-	-	-	-	-	-	[68]
DLP	3-pt	937±24	-	-	5	25x1.5x2	-	-	[2]
SLA	3-pt	845±124	-	-	-	-	-	-	[69]
SLA	3-pt	1000	-	-	-	25x4x1.2	X	-	[70]
SLA	3-pt	894.1	-	5.2	15	24x4x2	X	647	[59]
DLP	3-pt	831.5	-	4.9	15	24x4x2	X	595	[59]
DLP	3-pt	730±64	-	-	5	30x4x3	X	-	HINP*
DLP	4-pt	521±83	556	6.8	30	30x4x3	X	521	HINP*
DLP	4-pt	526±77	559	7.8	30	30x4x3	X	526	2SERA*

3.8 Surface roughness, trueness and sintering shrinkage

The obtained surface roughness was anisotropic for the HINP and 2SERA slurry-based ceramics, as summarised in Table 7. The top surface, i.e. the slurry side, had the lowest roughness of all orientations (0.35±0.11 µm). The bottom surface, i.e. the base plate side, had a slightly higher surface roughness of 0.66±0.37 µm due to remnants of the base layer. The deviation is slightly higher because the manual removal of the base layer depended on the sample and the position on the build platform. No significant differences were found between

HINP and 2SERA slurry-based ceramics for different top and bottom surfaces. Along the building direction, the highest surface roughness measured was 7.85±0.78 µm and 5.77±0.35 µm for HINP and 2SERA slurry-based ceramics, respectively. The addition of SERA to the slurry led to a decrease of these edge defects or side protrusions, but the layerwise build-up and smaller edge defects were still present. Sun *et al*. (2021) [16] reported an average surface roughness of 1.62±0.23 µm, 2.19±0.18 µm and 2.86±0.12 µm respectively for the top, side and bottom surface of DLP-produced 3Y-TZP. Paterlini *et al.* (2021) [71] reported an average surface roughness of 0.54 µm and 0.92 µm for the top and side surface, respectively, using a commercial 3Y-TZP slurry from Lithoz (Vienna, Austria). Comparing these values is difficult due to different measurement and analysis parameters, but it can be concluded that DLP-produced 3Y-TZP has an anisotropic roughness, with the highest roughness along the building direction.

After printing, the ceramics also showed an anisotropic trueness and after sintering an anisotropic shrinkage (Table 7). Slight inaccuracies in trueness of the green body in the in-plane (XY) direction were caused due to light scattering in the green body during printing. Adjusting the light intensity and exposure time, as well as the slurry composition could however improve the printing accuracy [40,72]. A higher deviation in trueness along the Z-axis was also observed, 3.3±0.5% for HINP prints and 3.6±0.5% for 2SERA prints respectively (Table 7), which can be linked to a higher polymerization shrinkage in the Z direction. The layerwise build-up could often cause anisotropic shrinkage of the green bodies. The anisotropic shrinkage after sintering could be partially caused by the inaccuracy after printing. Increasing the solid loading may improve the trueness and shrinkage anisotropy. In this study, shrinkage coefficients were taken into account to oversize the CAD files of the printed designs. Alternative solutions are predictive models for shrinkage, potentially resulting in more accurate sintered designs, especially for more complex structures [73]. Secondly, warping is a well-known cause of dimensional inaccuracy. Ensuring gradual temperature control during post-curing and debinding can minimize warpage. A potential solution for warping could also be a thermal annealing to decrease internal stresses in the sintered ceramic, although this can significantly alter the microstructure [14]

Table 7. Trueness of the printed green body and surface roughness and shrinkage of the sintered 3Y-TZP ceramics along the different building orientations. Negative values indicate excess material, positive values indicate lack of material.

Ceramic	Trueness green body (%)			Shrinkage (%)			Roughness (S_a, µm)		
	X	Y	Z	X	Y	Z	Top surface	Side surface	Bottom surface
HINP	2.2±1.5	3.5±0.5	-3.3±0.5	19.6±0.6	20.2±0.5	24.9±0.5	0.35±0.11	7.85±0.78	0.66±0.37
2SERA	1.3±2.0	1.3±2.0	-3.6±0.5	20.3±0.4	19.9±0.6	25.2±0.3	0.35±0.11	5.77±0.35	0.72±0.31

3.9 Printable wall thickness and some components

As shown in Figure 16, it is possible to accurately print wall thicknesses down to 500 µm using the 2SERA slurry with 48 vol% zirconia powder. Given a 19.6% shrinkage in the X-direction as reported in Table 7, this resulted in sintered walls of 400 µm. Although a smallest wall thickness of 100 µm could be printed, these parts are too fragile for manual washing and the final printed dimension is closer to 200 µm due to light scattering and concomitant overcuring. This shows the need to improve the green strength through adjusting the composition of the slurry, and the need to determine a minimal green strength necessary for post-processing DLP-produced 3Y-TZP. The higher inaccuracies for the smaller wall thicknesses of 100 µm and 250 µm were caused by light scattering. The voxel size of the printer was 50 µm, which could also have a small influence on the printing accuracy when the specific wall of the part is

not perfectly positioned over two voxels. The use of a lower intensity LED (10% LED intensity instead of 30%) with longer exposure times resulting in the same energy dose, actually decreased the dimensional accuracy of the ceramic. Longer exposure times seem more harmful that higher energy doses for scattering of the light. A lower powder load (40 vol%) did not significantly improve the printing accuracy, but the thinner walls held up better during cleaning due to the higher binder content. Figure 17 shows some printed and sintered components using the HINP slurry. It is possible to create complex and accurate designs with specific details.

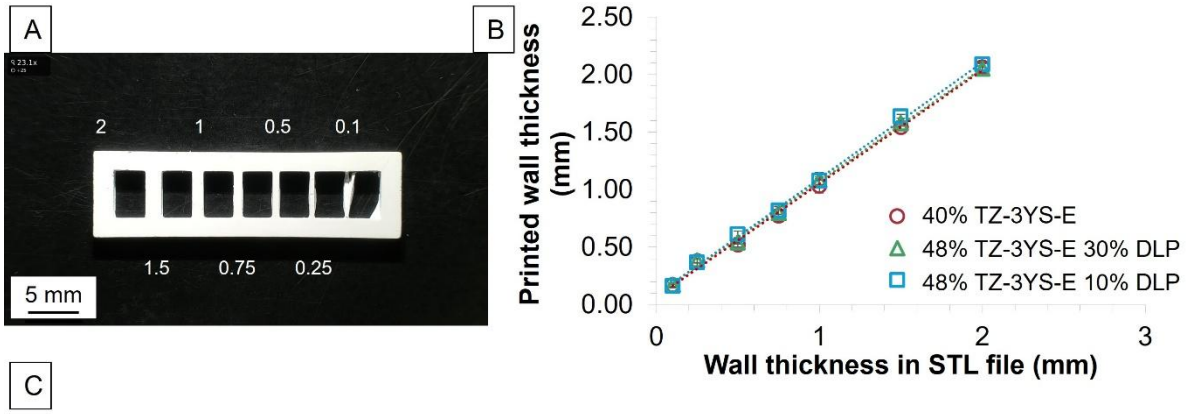

C

Wall thickness (mm)	0.1	0.25	0.5	0.75	1	1.5	2
40% TZ-3YS-E	0.17±0.02	0.38±0.02	0.56±0.02	0.77±0.06	1.03±0.06	1.54±0.02	2.06±0.04
48% TZ-3YS-E 30% DLP	0.18±0.01	0.39±0.02	0.54±0.03	0.80±0.04	1.09±0.01	1.58±0.01	2.05±0.04
48% TZ-3YS-E 10% DLP	0.16±0.02	0.37±0.03	0.61±0.03	0.82±0.03	1.08±0.03	1.64±0.02	2.09±0.03

Figure 16. (A) Printed green body indicating CAD wall thicknesses in mm. (B) Plot comparing the printed wall thickness with the STL file value of the wall thickness. The solid line gives the linear relationship, the plotted dots show the average measured value of five different green bodies. (C) Table with the numerical values of the effective printed wall thickness in the green body.

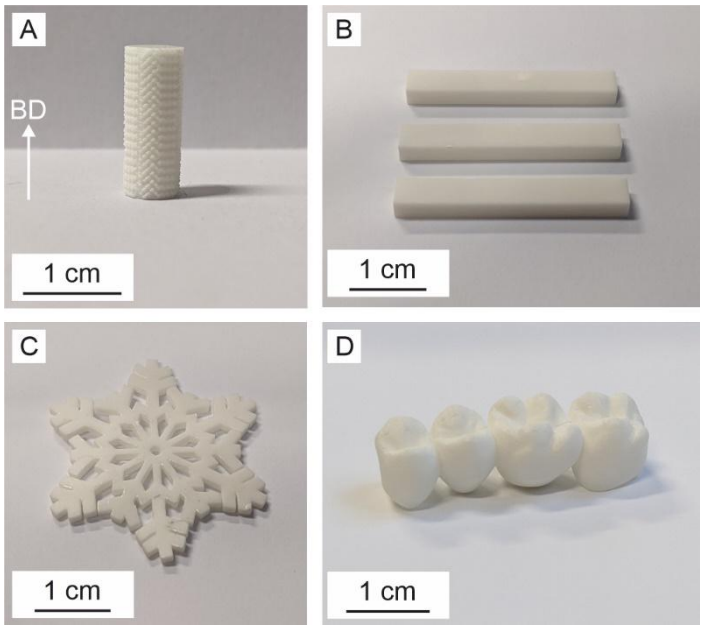

Figure 17. Sintered DLP ZrO_2 ceramics: (A) a partial implant with a complex surface layer and a dense core, (B) bending bars, (C) a snowflake gadget, and (D) a four-unit fixed dental prosthesis.

4. Conclusion

An acrylate-based 3Y-TZP slurry was developed starting from an equal weight HDDA, IBOA and NPDGA monomer mixture.

To improve powder stabilization and decrease the viscosity of the powder-monomer paste, 3 wt% Disperbyk-111 dispersant was found to be most efficient in lowering the viscosity below 10 Pa·s, while allowing to accommodate up to 48 vol% of 3Y-TZP powder, and providing sufficiently strong green bodies that securely adhere to the build platform.

In order to establish a crack-free thermal debinding cycle, the addition of PPG-400 with a thermal decomposition around 250°C was found to be most complementary to the monomer-dispersant mixture, with a thermal decomposition in the 350-525 °C window. In order to limit the viscosity increase and avoid crack formation during debinding, 25 wt% PPG-400 (relative to the monomer content of the slurry) was found to be optimal. A thermal debinding cycle was formulated, but since PPG-400 is water soluble, a combined water and thermal debinding is an alternative.

The addition of 2 wt% BYK-UV 3500 surface additive improved the wetting of the slurry and green bodies and decreased the size of the protrusions observed on the side of the printed green bodies. The surface additive also reduced the separation forces exerted on the prints during DLP.

The ultimate slurry developed in this work contained HDDA, IBOA, NGPDA monomers and PPG-400 diluent in a 1:1:1:1 weight ratio with a ZrO_2 solid loading of 48 vol% (84.5 wt%), 3 wt% Disperbyk-111 dispersant (relative to the solid loading) and 0.33 wt% BAPO photoinitiator (relative to the monomer content), with or without 2 wt% BYK-UV 3500 surface energy release agent (relative to the monomer + diluent content).

Bending bars with high trueness could be printed taking into account the polymerization shrinkage and the overcuring issues. In the XY-plane, excess material up to 3.5% could be cured, resulting in slight inaccuracies. Along the Z-axis, a higher deviation in trueness was observed in the Z direction (3.3%), potentially linked to polymerization shrinkage due to the layerwise build-up. The shrinkage after sintering was anisotropic, i.e. 25.2±0.3 % in the building (Z) direction and 20.1±0.5 % along the XY-direction. It was however possible to print ceramics with highly accurate dimensions, taking into account the anisotropic shrinkage factors. A wall thickness of 500 µm could accurately be printed and was able to withstand the following manual cleaning during post-processing. The surface roughness was anisotropic with an average surface roughness S_a of 5.77±0.35 µm along the building direction, where the layerwise build-up could still be observed. The top and bottom surfaces had a S_a as low as 0.35±0.11 µm and 0.66±0.37 µm, respectively.

The near fully dense (99.8% TD) sintered prints had a Vickers hardness, indentation fracture resistance and Young's modulus of V_H = 12.9±0.1 GPa, K_{ind} = 4.0±0.01 MPa $m^{1/2}$ and E = 206 GPa respectively, comparable to conventionally manufactured 3Y-TZP. A 3-pt bending strength of σ_m = 730±64 MPa or 4-pt bending strength of σ_{m4pt} = 521±83 MPa were obtained with the optimized HINP slurry using a printing layer thickness of 15 µm, an energy dose of 30.4 mJ/cm^2 and a curing depth around 75 µm. The addition of 2 wt% BYK-UV 3500 did not increase the 4-pt bending strength (526±77 MPa), but slightly increased the Weibull modulus from 6.8 to 7.8. The limited bending strength is due to the presence of trapped pores inside the layers, surface defects due to manual handling or remaining base layer particles, and edge defects due to overcuring and DLP separation forces.

Acknowledgements

This research was supported by the Research Fund of KU Leuven (projects KA/16/126, C24/17/084 and C24E/23/037), and the Fund for Scientific Research - Flanders (FWO Vlaanderen) (grant number G.0431.10N). F. Zhang thanks the Scientific Research - Flanders (FWO-Vlaanderen) for her grant G057924N. The authors acknowledge the financial support from the FWO – Vlaanderen through the Medium-Scale Research Infrastructure project COMPLEXURF (I009220N) for the Sensofar equipment. The authors thank Dr. Merve Aktan for her help with the contact angle measurements.

Bibliography

[1] J. Chevalier, L. Gremillard, Ceramics for medical applications: A picture for the next 20 years, J Eur Ceram Soc 29 (2009) 1245–1255. https://doi.org/10.1016/j.jeurceramsoc.2008.08.025.

[2] C. Yang, W. Wu, Z. Fu, H. Zheng, Preparation and thermal insulation properties of TPMS 3Y-TZP ceramics using DLP 3D printing technology, J Mater Sci 58 (2023) 11992–12007. https://doi.org/10.1007/s10853-023-08749-0.

[3] A.C. Branco, R. Colaço, C.G. Figueiredo-Pina, A.P. Serro, Recent Advances on 3D-Printed Zirconia-Based Dental Materials: A Review, Materials 16 (2023) 1860. https://doi.org/10.3390/ma16051860.

[4] P. Sengupta, A. Bhattacharjee, H.S. Maiti, Zirconia: A Unique Multifunctional Ceramic Material, Transactions of the Indian Institute of Metals 72 (2019) 1981–1998. https://doi.org/10.1007/s12666-019-01742-9.

[5] M. Revilla-León, M. Sadeghpour, M. Özcan, An update on applications of 3D printing technologies used for processing polymers used in implant dentistry, Odontology 108 (2020) 331–338. https://doi.org/10.1007/s10266-019-00441-7.

[6] M. Carlotti, V. Mattoli, Functional Materials for Two-Photon Polymerization in Microfabrication.pdf, Small 15 (2019) 1902687. https://doi.org/10.1002/smll.201902687.

[7] S. Saleh Alghamdi, S. John, N. Roy Choudhury, N.K. Dutta, Additive Manufacturing of Polymer Materials: Progress, Promise and Challenges, (2021). https://doi.org/10.3390/polym13.

[8] R. Van Noort, The future of dental devices is digital, Dental Materials 28 (2012) 3–12. https://doi.org/10.1016/j.dental.2011.10.014.

[9] C.-Y. Liaw, M. Guvendiren, Current and Emerging Applications of 3D Printing in Restorative Dentistry, Biofabrication 9 (2017) 024102. https://doi.org/10.1007/s40496-018-0181-3.

[10] J. Wilkes, Y.C. Hagedorn, W. Meiners, K. Wissenbach, Additive manufacturing of ZrO2-Al2O3 ceramic components by selective laser melting, Rapid Prototyp J 19 (2013) 51–57. https://doi.org/10.1108/13552541311292736.

[11] K. Shahzad, J. Deckers, Z. Zhang, J.P. Kruth, J. Vleugels, Additive manufacturing of zirconia parts by indirect selective laser sintering, J Eur Ceram Soc 34 (2014) 81–89. https://doi.org/10.1016/j.jeurceramsoc.2013.07.023.

[12] Q. Liu, Y. Danlos, B. Song, B. Zhang, S. Yin, H. Liao, Effect of high-temperature preheating on the selective laser melting of yttria-stabilized zirconia ceramic, J Mater Process Technol 222 (2015) 61–74. https://doi.org/10.1016/j.jmatprotec.2015.02.036.

[13] M. Revilla-Léon, M. Özcan, Additive manufacturing technologies used for processing polymers: Current status and potential application in prsthetic dentistry, Journal of Prosthodontics 28 (2018) 146–158.

[14] Q. Arshad, M. Saqib, M.A. Arshad, M. Raza, M.I. Hussain, A. Asghar, X. Luo, Z. Chen, Progress in vat photopolymerisation additive manufacturing of ceramic lattice structures and applications, Thin-Walled Structures 209 (2025) 112918. https://doi.org/10.1016/j.tws.2025.112918.

[15] M.L. Griffith, Halloran John W., Freeform fabrication of ceramics via stereolithography, Journal of The American Ceramic Society 79 (1996) 2601–2608. https://doi.org/10.1111/j.1151-2916.1996.tb09022.x.

[16] J. Sun, X. Chen, J. Wade-Zhu, J. Binner, J. Bai, A comprehensive study of dense zirconia components fabricated by additive manufacturing, Addit Manuf 43 (2021) 101994. https://doi.org/10.1016/j.addma.2021.101994.

[17] A. Licciulli, C. Esposito Corcione, A. Greco, V. Amicarelli, A. Maffezzoli, Laser stereolithography of ZrO2 toughened Al2O3, J Eur Ceram Soc 25 (2005) 1581–1589. https://doi.org/10.1016/j.jeurceramsoc.2003.12.003.

[18] A.M. Knapp, J.W. Halloran, Binder removal from ceramic-filled thermoplastic blends, Journal of the American Ceramic Society 89 (2006) 2776–2781. https://doi.org/10.1111/j.1551-2916.2006.01179.x.

[19] J. Kim, C.W. Gal, Y.J. Choi, H. Park, S.Y. Yoon, H. suk Yun, Effect of non-reactive diluent on defect-free debinding process of 3D printed ceramics, Addit Manuf 67 (2023). https://doi.org/10.1016/j.addma.2023.103475.

[20] R. Ding, Y. Du, R.B. Goncalves, L.F. Francis, T.M. Reineke, Sustainable near UV-curable acrylates based on natural phenolics for stereolithography 3D printing, Polym Chem 10 (2019) 1067–1077. https://doi.org/10.1039/c8py01652f.

[21] R.B. Osman, A.J. van der Veen, D. Huiberts, D. Wismeijer, N. Alharbi, 3D-printing zirconia implants; a dream or a reality? An in-vitro study evaluating the dimensional accuracy, surface topography and mechanical properties of printed zirconia implant and discs, J Mech Behav Biomed Mater 75 (2017) 521–528. https://doi.org/10.1016/j.jmbbm.2017.08.018.

[22] W. Harrer, M. Schwentenwein, T. Lube, R. Danzer, Fractography of zirconia-specimens made using additive manufacturing (LCM) technology, J Eur Ceram Soc 37 (2017) 4331–4338. https://doi.org/10.1016/j.jeurceramsoc.2017.03.018.

[23] M. Saâdaoui, F. Khaldoun, J. Adrien, H. Reveron, J. Chevalier, X-ray tomography of additive-manufactured zirconia: Processing defects – Strength relations, J Eur Ceram Soc 40 (2020) 3200–3207. https://doi.org/10.1016/j.jeurceramsoc.2019.04.010.

[24] Y. Lu, Z. Mei, J. Zhang, S. Gao, X. Yang, B. Dong, L. Yue, H. Yu, Flexural strength and Weibull analysis of Y-TZP fabricated by stereolithographic additive manufacturing and

subtractive manufacturing, J Eur Ceram Soc 40 (2020) 826–834. https://doi.org/10.1016/j.jeurceramsoc.2019.10.058.

[25] H. Nakai, M. Inokoshi, K. Nozaki, K. Komatsu, S. Kamijo, H. Liu, S. Minakuchi, J. Vleugels, F. Zhang, B. Van Meerbeek, Additive manufactured zirconia in anticipation of dental applications, Materials 14 (2021). https://doi.org/10.3390/xxxxx.

[26] Q. Lian, X. Wu, D. Li, X. He, J. Meng, X. Liu, Z. Jin, Accurate printing of a zirconia molar crown bridge using three-part auxiliary supports and ceramic mask projection stereolithography, Ceram Int 45 (2019) 18814–18822. https://doi.org/10.1016/j.ceramint.2019.06.111.

[27] W. Wang, H. Yu, Y. Liu, X. Jiang, B. Gao, Trueness analysis of zirconia crowns fabricated with 3-dimensional printing, Journal of Prosthetic Dentistry 121 (2019) 285–291. https://doi.org/10.1016/j.prosdent.2018.04.012.

[28] W. Wang, J. Sun, Dimensional accuracy and clinical adaptation of ceramic crowns fabricated with the stereolithography technique, Journal of Prosthetic Dentistry 125 (2021) 657–663. https://doi.org/10.1016/j.prosdent.2020.02.032.

[29] M. Revilla-León, M.M. Methani, D. Morton, A. Zandinejad, Internal and marginal discrepancies associated with stereolithography (SLA) additively manufactured zirconia crowns, Journal of Prosthetic Dentistry 124 (2020) 730–737. https://doi.org/10.1016/j.prosdent.2019.09.018.

[30] Q. Lian, W. Sui, X. Wu, F. Yang, S. Yang, Additive manufacturing of ZrO2 ceramic dental bridges by stereolithography, Rapid Prototyp J 24 (2018) 114–119. https://doi.org/10.1108/RPJ-09-2016-0144.

[31] P.F. Jacobs, Rapid Prototyping & Manufacturing: Fundamentals of Stereolithography, Dearborn, Michigan, 1992. https://doi.org/10.1016/0278-6125(93)90311-g.

[32] D. Yang, H. Conrad, Enhanced sintering rate and finer grain size in yttria-stablized zirconia (3Y-TZP) with combined DC electric field and increased heating rate, Materials Science and Engineering A 528 (2011) 1221–1225. https://doi.org/10.1016/j.msea.2010.10.041.

[33] ISO 4288: Geometrical Product Specifications (GPS) - Surface texture: Profile method - Rules and procedures for the assessment of surface texture, (1996).

[34] DIN 4768: Determination of values of surface roughness parameters Ra. Rz, Rmax using electrical contact (stylus) instruments Concepts and measuring conditions, 1990 (n.d.).

[35] J.F. Archard, W. Hirst, The wear of metals under unlubricated conditions, in: Proceedings of the Royal Society of London A: Mathematical and Physical Sciences, 1956: pp. 397–410.

[36] H.-J. Hu, W.-J. Huang, Studies on wears of ultrafine-grained ceramic tool and common ceramic tool during hard turning using archard wear model, The International Journal of Advanced Manufacturing Technology 69 (2013) 31–39.

[37] ASTM E1876-01: Standard Test Method for Dynamic Young's Modulus, Shear Modulus, and Poisson's Ratio by Impulse Excitation of Vibration, 2005.

[38] G.R. Anstis, P. Chantikul, B.R. Lawn, D.B. Marshall, A Critical Evaluation of Indentation Techniques for Measuring Fracture Toughness: I, Direct Crack Measurements, Journal of the American Ceramic Society 64 (1981) 533–538. https://doi.org/10.1111/j.1151-2916.1981.tb10320.x.

[39] A. Tsetsekou, C. Agrafiotis, A. Milias, Optimization of the rheological properties of alumina slurries for ceramic processing applications Part I: Slip-casting, J Eur Ceram Soc 21 (2001) 363–373. https://doi.org/10.1016/S0955-2219(00)00185-0.

[40] J. Sun, J. Binner, J. Bai, Effect of surface treatment on the dispersion of nano zirconia particles in non-aqueous suspensions for stereolithography, J Eur Ceram Soc 39 (2019) 1660–1667. https://doi.org/10.1016/j.jeurceramsoc.2018.10.024.

[41] E. Johansson, O. Lidström, J. Johansson, O. Lyckfeldt, E. Adolfsson, Influence of resin composition on the defect formation in alumina manufactured by stereolithography, Materials 10 (2017). https://doi.org/10.3390/ma10020138.

[42] R. Bjørk, V. Esposito, E.M. Lauridsen, P.S. Jørgensen, J.L. Fife, K.B. Andersen, S.P.V. Foghmoes, N. Pryds, In situ characterization of delamination and crack growth of a CGO-LSM multi-layer ceramic sample investigated by X-ray tomographic microscopy, J Eur Ceram Soc 34 (2014) 3019–3025. https://doi.org/10.1016/j.jeurceramsoc.2014.04.029.

[43] B. Aktas, R. Das, A. Acikgoz, G. Demircan, S. Yalcin, H.G. Aktas, M.V. Balak, DLP 3D printing of TiO2-doped Al2O3 bioceramics: Manufacturing, mechanical properties, and biological evaluation, Mater Today Commun 38 (2024) 107872. https://doi.org/10.1016/j.mtcomm.2023.107872.

[44] M. Li, W. Liu, J. Nie, C. Wang, W. Li, Z. Xing, Influence of yttria-stabilized zirconia content on rheological behavior and mechanical properties of zirconia-toughened alumina fabricated by paste-based stereolithography, J Mater Sci 56 (2021) 2887–2899. https://doi.org/10.1007/s10853-020-05494-6.

[45] M. Pfaffinger, M. Hartmann, M. Schwentenwein, J. Stampfl, Stabilization of tricalcium phosphate slurries against sedimentation for stereolithographic additive manufacturing and influence on the final mechanical properties, Int J Appl Ceram Technol 14 (2017) 499–506. https://doi.org/10.1111/ijac.12664.

[46] X. Song, Y. Chen, T.W. Lee, S. Wu, L. Cheng, Ceramic fabrication using Mask-Image-Projection-based Stereolithography integrated with tape-casting, J Manuf Process 20 (2015) 456–464. https://doi.org/10.1016/j.jmapro.2015.06.022.

[47] J.H. Lee, R.K. Prud'homme, I.A. Aksay, Cure depth in photopolymerization: Experiments and theory, 2001.

[48] A. Alamdari, J. Lee, M. Kim, M.O.F. Emon, A. Dhinojwala, J.W. Choi, Effects of Surface Energy Reducing Agents on Adhesion Force in Liquid Bridge Microstereolithography, Addit Manuf 36 (2020). https://doi.org/10.1016/j.addma.2020.101522.

[49] X. Liang, Q. Li, B. Qu, Y. Qiu, S. Liu, Q. Wang, J. Liang, H. Tan, Y. Liu, J. Li, High-precision and high-strength SiC ceramic green body by stereolithography: Slurry design and defect control, J Alloys Compd 1035 (2025) 180860. https://doi.org/10.1016/j.jallcom.2025.180860.

[50] A. Licciulli, C. Esposito Corcione, A. Greco, V. Amicarelli, A. Maffezzoli, Laser stereolithography of ZrO2 toughened Al2O3, J Eur Ceram Soc 25 (2005) 1581–1589. https://doi.org/10.1016/j.jeurceramsoc.2003.12.003.

[51] A. Liebermann, A. Schultheis, F. Faber, P. Rammelsberg, S. Rues, F.S. Schwindling, Impact of post printing cleaning methods on geometry, transmission, roughness parameters, and flexural strength of 3D-printed zirconia, Dental Materials 39 (2023) 625–633. https://doi.org/10.1016/j.dental.2023.05.005.

[52] J. Sun, J. Binner, J. Bai, 3D printing of zirconia via digital light processing: optimization of slurry and debinding process, J Eur Ceram Soc 40 (2020) 5837–5844. https://doi.org/10.1016/j.jeurceramsoc.2020.05.079.

[53] H. Li, Y. Liu, Y. Liu, Q. Zeng, K. Hu, Z. Lu, J. Liang, Effect of debinding temperature under an argon atmosphere on the microstructure and properties of 3D-printed alumina ceramics, Mater Charact 168 (2020) 110548. https://doi.org/10.1016/j.matchar.2020.110548.

[54] M. Trunec, Z. Chlup, Higher fracture toughness of tetragonal zirconia ceramics through nanocrystalline structure, Scr Mater 61 (2009) 56–59. https://doi.org/10.1016/j.scriptamat.2009.03.019.

[55] L. Ruiz, M.J. Readey, Effect of Heat Treatment on Grain Size, Phase Assemblage, and Mechanical Properties of 3 mol% Y-TZP, Journal of the American Ceramic Society 79 (1996) 2331–2340. https://doi.org/10.1111/j.1151-2916.1996.tb08980.x.

[56] C. Marsico, M. Øilo, J. Kutsch, M. Kauf, D. Arola, Vat polymerization-printed partially stabilized zirconia: Mechanical properties, reliability and structural defects, Addit Manuf 36 (2020). https://doi.org/10.1016/j.addma.2020.101450.

[57] M. Borlaf, A. Serra-Capdevila, C. Colominas, T. Graule, Development of UV-curable ZrO2 slurries for additive manufacturing (LCM-DLP) technology, J Eur Ceram Soc 39 (2019) 3797–3803. https://doi.org/10.1016/j.jeurceramsoc.2019.05.023.

[58] R. Belli, U. Lohbauer, The breakdown of the Weibull behavior in dental zirconias, Journal of the American Ceramic Society 104 (2021) 4819–4828. https://doi.org/10.1111/jace.17886.

[59] Z. Zhai, C. Qian, T. Jiao, C. Xu, J. Sun, Zirconia specimens printed by vat photopolymerization: Mechanical properties, fatigue properties, and fractography analysis, Journal of Prosthodontics (2024). https://doi.org/10.1111/jopr.13942.

[60] W. Li, M. Liu, W. Liu, H. Zhou, M. Li, Y. Chen, Z. Xing, High-performance integrated manufacturing of a 3Y-TZP ceramic crown through viscoelastic paste-based vat photopolymerization with a conformal contactless support, Addit Manuf 59 (2022). https://doi.org/10.1016/j.addma.2022.103143.

[61] K.J. Jang, J.H. Kang, J.G. Fisher, S.W. Park, Effect of the volume fraction of zirconia suspensions on the microstructure and physical properties of products produced by additive manufacturing, Dental Materials 35 (2019) e97–e106. https://doi.org/10.1016/j.dental.2019.02.001.

[62] K. Zhang, R. He, G. Ding, C. Feng, W. Song, D. Fang, Digital light processing of 3Y-TZP strengthened ZrO2 ceramics, Materials Science and Engineering A 774 (2020). https://doi.org/10.1016/j.msea.2019.138768.

[63] M. Shen, W. Zhao, B. Xing, Y. Sing, S. Gao, C. Wang, Z. Zhao, Effects of exposure time and printing angle on the curing characteristics and flexural strength of ceramic samples fabricated via digital light processing, Ceram Int 46 (2020) 24379–24384. https://doi.org/10.1016/j.ceramint.2020.06.220.

[64] M. Revilla-León, N. Al-Haj Husain, L. Ceballos, M. Özcan, Flexural strength and Weibull characteristics of stereolithography additive manufactured versus milled zirconia, Journal of Prosthetic Dentistry (2020) 1–6. https://doi.org/10.1016/j.prosdent.2020.01.019.

[65] B. Coppola, T. Lacondemine, C. Tardivat, L. Montanaro, P. Palmero, Designing alumina-zirconia composites by DLP-based stereolithography: Microstructural tailoring and mechanical performances, Ceram Int 47 (2021) 13457–13468. https://doi.org/10.1016/j.ceramint.2021.01.204.

[66] M. Bergler, J. Korostoff, L. Torrecillas-Martinez, F. Mante, Ceramic Printing—Comparative Study of the Flexural Strength of 3D-Printed and Milled Zirconia, Int J Prosthodont (2021). https://doi.org/10.11607/ijp.6749.

[67] M.-S. Kim, M.-H. Hong, B.-K. Min, Y.-K. Kim, H.-J. Shin, T.-Y. Kwon, Microstructure, Flexural Strength, and Fracture Toughness Comparison between CAD/CAM Milled and 3D-Printed Zirconia Ceramics, Applied Sciences 12 (2022) 9088. https://doi.org/10.3390/app12189088.

[68] Y. Liu, Y. Liu, W. She, Y. Cao, Q. Zeng, N. Dong, Effect of reactive diluent concentration on rheological and curing behavior of zirconia ceramic slurry for DLP printing, Int J Appl Ceram Technol 21 (2024) 62–75. https://doi.org/10.1111/ijac.14493.

[69] H. Gong, C. Wang, H. Wu, X. Luo, J. Liang, N. Li, S. Chen, Y. Long, Investigating the correlation and composition of organic components in ZrO2-based slurry on printability improvement and defect suppression of Vat photopolymerization, Mater Today Commun 34 (2023). https://doi.org/10.1016/j.mtcomm.2022.105149.

[70] S. Miura, A. Shinya, Y. Ishida, T. Fujita, P. Vallittu, L. Lassila, M. Fujisawa, The effect of low-temperature degradation and building directions on the mechanical properties of additive-manufactured zirconia, Dent Mater J 42 (2023) 800–805. https://doi.org/10.4012/dmj.2023-089.

[71] A. Paterlini, A. Stamboulis, V. Turq, R. Laloo, M. Schwentenwein, D. Brouczek, M. Piccinini, G. Bertrand, Lithography-based manufacturing of advanced ceramics for orthopaedic applications: A comparative tribological study, Open Ceramics 8 (2021). https://doi.org/10.1016/j.oceram.2021.100170.

[72] C. Goutagny, S. Hocquet, D. Hautcoeur, M. Lasgorceix, N. Somers, A. Leriche, Development of calcium phosphate suspensions suitable for the stereolithography process, Open Ceramics 7 (2021). https://doi.org/10.1016/j.oceram.2021.100167.

[73] Y. Wang, Z. Wang, X. Yu, Z. Yu, K. Zhong, Y. Zhao, J. Zhao, Predicting dimensional deviation for sintering-induced shrinkage of Al2O3 ceramics manufactured by vat

photopolymerization: Using convolutional neural network, Mater Today Commun 37 (2023) 107309. https://doi.org/10.1016/j.mtcomm.2023.107309.

Supplemental information

S1. Extra results of slurry characterization

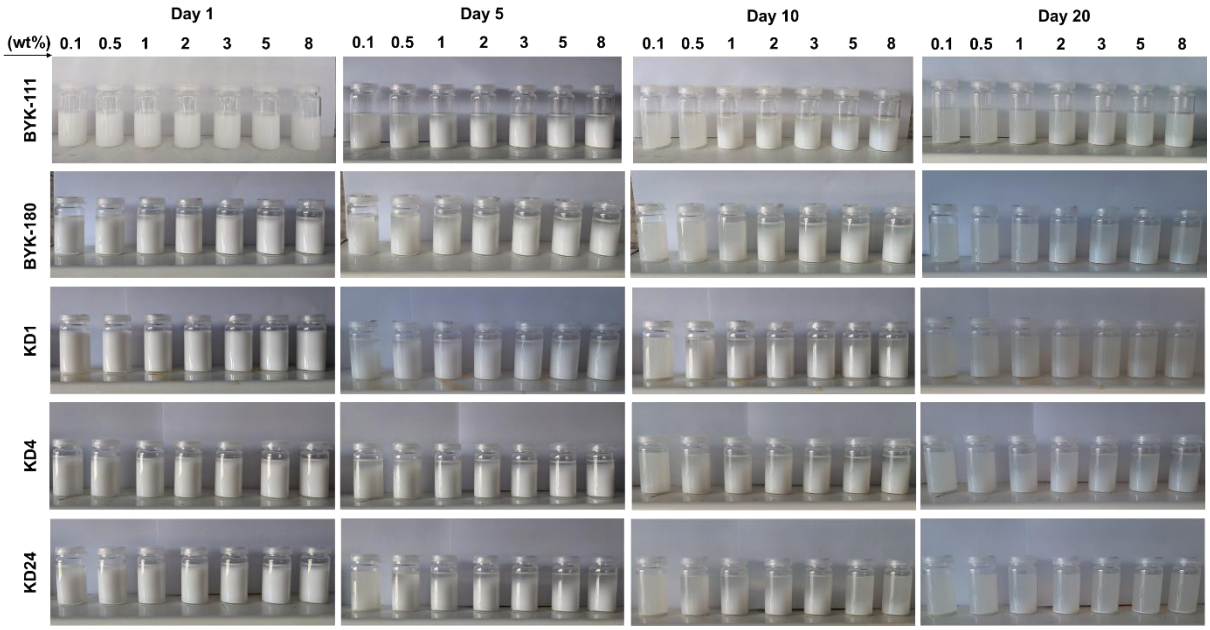

Figure S1. Overview of the sedimentation vials of diluted slurries containing <1 vol% of 3Y-TZP with varying amounts (0.1-8 wt% relative to the powder load) of Disperbyk-111, Disperbyk-180, KD1, KD4, and KD24 dispersants as a function of time.

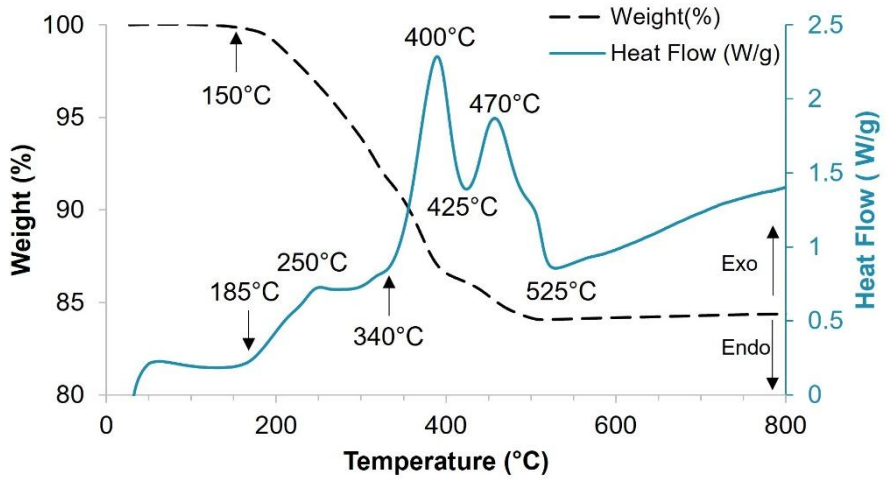

Figure S2. TGA/DSC curve of the HINP slurry.

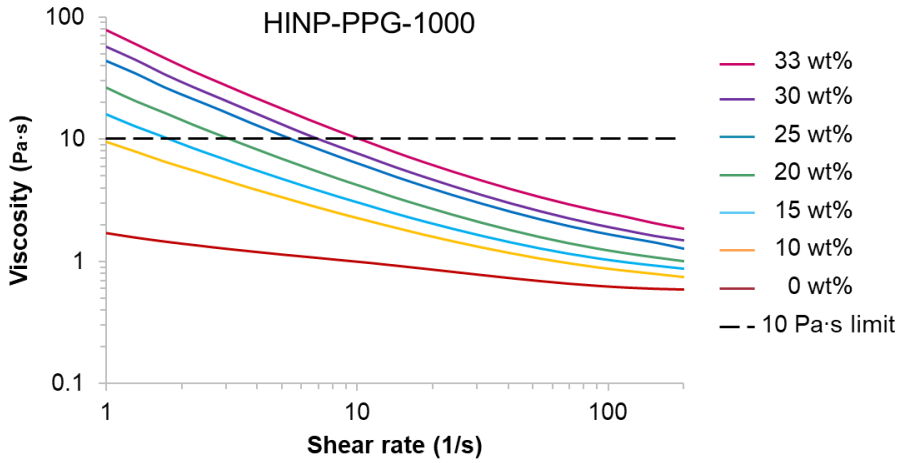

Figure S3. Flow sweeps of 40 vol% 3Y-TZP loaded slurries containing 0-33 wt% PPG-1000.

S2. Comparison of strength data in literature

To roughly compare the strength values reported in literature with the flexural strength obtained in this work, strength scaling of all data was performed. The selected reference sample size had a cross-section of 3x4 mm^2 using an outer span of 20 mm in the 4-point bending setup, i.e. the setup that was used to perform the flexural tests in this work. The following conversion formula was used to calculate the scaled average 4-point bending strength for all the reported data:

$$\sigma_{4pt} = \left[\left(\frac{b_{3pt}h_{3pt}L_{3pt}}{b_{4pt}h_{4pt}L_{4pt}}\right)\frac{2}{m+2}\right]^{1/m} \cdot \sigma_{3pt}$$

with b the width and h the height of the bending bar, L the span length, and m the Weibull modulus.

Using this formula, the measured 4-point bending strength from this work can be converted into the 3-point bending strength, resulting in an average 3-point bending strength of 648 MPa and 654 MPa for the HINP and 2SERA slurry-based ceramics, respectively. This is substantially lower than the strength of 730±64 MPa measured for HINP.

An overview of the nomenclature of the printing orientation of the bending bars and mechanical performance data presented in this paper is provided in Figure S4.

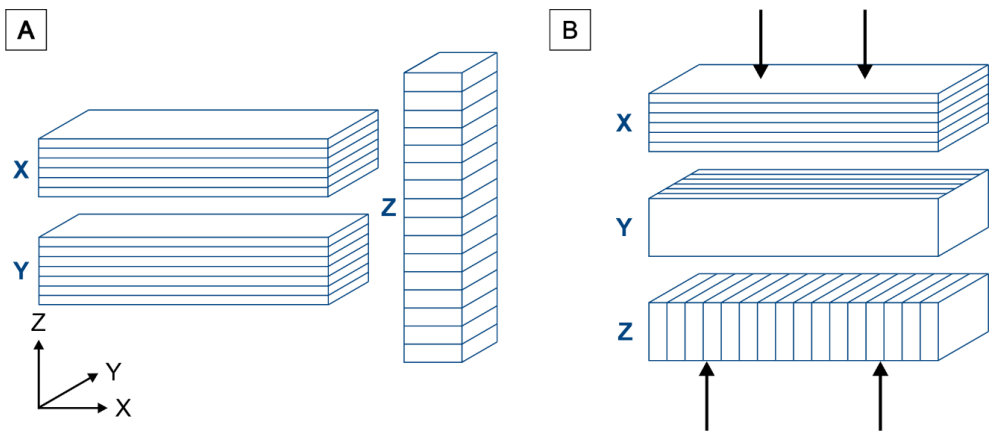

Figure S4. (A) Printing and (B) loading directions with the nomenclature of the samples used for mechanical characterization.